Assessment of Basin-Scale Hydrologic Impacts of CO_2 Sequestration, Illinois Basin

Mark Person*[1], Amlan Banerjee[1], John Rupp[2], Cristian Medina[2], Peter Lichtner[3], Carl Gable[3], Rajesh Pawar[3], Michale Celia[4], Jennifer McIntosh[5], Victor Bense[6]

1. New Mexico Institute of Mining and Technology, Department of Earth & Environmental Science, 801 Leroy Place, Socorro, NM 87801, USA.

2. Indiana Geological Survey, Indiana University, 611 North Walnut Grove, Bloomington, IN 47405-2208, USA.

3. Los Alamos National Laboratory, EES-16, Las Alamos, NM 87545, USA.

4. Princeton University, Department of Civil Engineering, E-208 E-Quad, Princeton, NJ 08544, USA.

5. University of Arizona, Department of Hydrology and Water Resources, 1133 E. James E. Rogers Way, Tucson, Arizona 85716, USA.

6. School of Environmental Sciences, University of East Anglia, Norwich, NR4 7TJ, England.

Submitted to Greenhouse Gas Control Journal

June 26, 2009

*Corresponding author: New Mexico Institute of Mining and Technology; Department of Earth & Environmental Science; 801 Leroy Place; Socorro, NM 87801. Tel: 001-575- 835-6506; fax: 001-575-835-6436;
E-mail address: mperson@nmt.edu

Abstract

Finite-element based sharp-interface models of CO_2 injection were constructed for the Illinois Basin in which porosity and permeability were varied with depth from 0.2 to 0.05 and 125 to 5 mD, respectively within the Mount Simon Formation. We used 726 injection wells located near 42 power plants to deliver 80 million metric tons of CO_2/year. After 100 years of continuous injection, deviatoric fluid pressures varied between 4.4 to 16.4 MPa across central and southern part of the Illinois Basin. Maximum deviatoric pressure reached about 46 % of lithostatic levels to the south. The pressure disturbance (> 0.03 MPa) propagated 9-13 km away from the injection wells resulting in significant well-well pressure interference. The CO_2 plumes radial footprint was only 0.5-2 km after 100 years of injection. Net lateral brine displacement was insignificant due to leakage across the Eau Claire confining unit. If CO_2 remains in a separate phase on geologic time scales, it would migrate northward due to buoyancy at a rate of about 6m/1000 years. Because of historic and paleoseismic events in this region, care should be taken to avoid high pore pressures in the southern Illinois Basin. **(189 words)**

Keywords: Mount Simon, Illinois Basin, CO_2, earthquakes, pressure, brine transport

1. Introduction

The Illinois Basin hosts dozens of coal fired power plants which generates about 300 million metric tons (MT) of CO_2 annually (Fig. 1). As part of the Department of Energy's Geological Sequestration Regional Partnership program, the Midwest Geological Sequestration Consortium (MGSC), a partnership that includes the three state geological surveys in the Illinois basin is investigating the technical constraints on the injection of CO_2 into deep (>1.5 km) reservoirs under supercritical conditions. The Mount Simon Sandstone, a Cambrian siliciclastic unit that is present throughout the basin, is a saline water filled aquifer that is a candidate reservoir for geological sequestration. At these depths, the Mount Simon pore fluids are often in excess of 100,000 mg/l (Hanor, 1987; Hanor and McIntosh, 2006). Simple back of the envelope calculation suggests that there is adequate pore space to accommodate this amount of annual CO_2 production. Assuming that CO_2 is emplaced as a supercritical fluid having a density of 500 kg/m^3 into a 500m thick Mount Simon sandstone having an average porosity of 10%, 80 million metric tons of CO_2 could displace all of the brines from an area surrounding a well field and would have an approximate aerial footprint of about 1.8 km x 1.8 km each year. Assuming a simple geometry for the Mount Simon and Illinois basin (500 km by 600 km by 500m), this volume of CO_2 injection would result in the displacement of brines out of the center of the Illinois basin towards its outer margins at a rate of about 0.003 m/year. This calculation doesn't account for more rapid solute migration along permeable pathways (e.g. Liu et al. 2004) and must be considered as a minimum estimate.

It is critical to ensure that fluid pressures near the CO_2 injection wells do not exceed 80% of lithostatic levels in order to minimize the potential of hydrofracturing of the overlying Eau Claire confining unit or inducing earthquakes (e.g. Hsieh and Bredehoeft, 1981; Nicholson and Wesson, 1980, Zoback and Harjes, 1997). This is particularly important for the southern Illinois Basin which hosts active seismogenic zones including the Wabash Valley and New Madrid Seismic Zones (Fig. 2A; Eager et al. 2006, Cramer et al. 1992). Carbon-14 dating of sand dikes and other liquefaction features near fault zones suggests that a series of high magnitude (M5-7) earthquakes occurred during the Holocene

97 across the southern Illinois Basin (Wheeler and Cramer, 2002; Obermeier et al. 1992; Munson et al.,
98 1992; Fig. 2A). The largest historic earthquake on North America is associated with the Reelfoot Rift
99 system (New Madrid Seismic Zone) which northern margin extends into the southern Illinois Basin.
100 Eager et al. (2006) suggest that the tight clustering of recent micro-earthquakes (~ M1.1) along the
101 Wabash Valley Seismic zone may be due to secondary injection of water associated with water floods
102 within the Illinois Basin. Several seismic events (M4.3-M2.8) are believed to be the result of 11 MPa
103 of induced pore pressure associated with pumping of 164 m^3/day of hazardous waste into a Class-1
104 injection into the a basal Paleozoic reservoir (not the Mount Simon Formation) in Ohio (Fig. 2B;
105 Nicholson and Wesson, 1980; Nicholson et al. 1988 ; Seeber et al. 2004). These authors report that
106 these earthquakes occurred 2 km below Mount Simon formation along a previously unmapped
107 Precambrian fault zone. What is troubling is that the induced pore pressures were far below
108 lithostatic levels and that some of the faults within the southern Illinois Basin (Dudzek et al. 2004) are
109 sub-parallel to the maximum horizontal compressive stress direction (bold blue lines, Fig. 2B)
110 (Zoback and Hickman, 1982; Zoback and Zoback, 1989).
111
112 There are reasons to be concerned that pore pressures could approach the lithostatic pressure (fracture
113 pressure) as a result of large scale CO_2 injection within the Mount Simon. First, the average
114 permeability of this Cambrian, Mount Simon reservoir is moderate (less than 1000 mD) and decreases
115 with depth as discussed below. Second, 20th century water withdraws from Illinois Basin Cambro-
116 Ordovican aquifer system (which includes the Mount Simon Formation; Walton, 1962) resulted in
117 large regions (50 km by 50 km) of significant sub-hydrostatic fluid pressures (Olcott, 1992) around
118 Chicago (Fig. 3) due to freshwater withdraws and Minneapolis/St. Paul (Lindholm, 1990; Lloyd and
119 Lyke, 1995). The annual withdraws from municipal water supply wells from the Mount Simon
120 aquifer beneath cities of Minneapolis/St Paul (e.g. 277 million metric tons of H_2O; Fig. 3C) are of the
121 same order of magnitude as the mass of CO_2 generated across the Illinois Basin by coal-fired power
122 plants. Over the past several decades, water withdraws have modified regional groundwater flow
123 patterns and resulted in decrease of as much as 45 m (0.45 MPa) in the Mount Simon sandstone

potentiometric surface in a limited area around the Twin Cities of Minneapolis/St. Paul and by over 182 m (1.8 MPa) in the Chicago area (Fig. 3A). Would CO_2 injection from more regionally distributed power plants result in comparable increases in heads and modification in groundwater flow directions? While CO_2 injection would presumably occur over a much more distributed area, the Mount Simon is probably less permeable to the south of Chicago where many coal-fired power plants are located.

The purpose of this study is to assess some of the hydrologic and seismogenic consequences of CO_2 injection into the Mount Simon Formation at the sedimentary basin scale. While a number of studies have quantified the effects of CO_2 injection into subsurface reservoirs around the world (e.g. Chadwick et al., 2003; Hovorka et al., 2001; Lu and Lichtner, 2007), these studies have focused on localized regions (up to about 10 km by 10 km by 100m in the x- ,y-, and z-directions, respectively) around injection wells and have neglected the impact of injection on the regional flow field. With only one exception (Birkholzer et al. 2007), we are aware of no quantitative models that have been developed to consider the consequences of large-scale CO_2 injection at the sedimentary basin scale. A secondary objective of this study is to demonstrate the efficacy of numerical sharp-interface representations of CO_2 injection. We propose to address several; specific issues regarding basin-scale CO_2 injection in this study:

1. Will large-scale CO_2 injection result in the generation of near lithostatic pressures in relatively low permeability regions of the Mount Simon Sandstone reservoir or will pressure anomalies be mitigated by leakage across the overlying Eau Claire confining unit?
2. What is the likely radius of pressure disturbance away from CO_2 injection wells? Will there be significant well-well interference within- or between- injection well centers?
3. Does CO_2 injection result in significant displacement of brines towards the margins of the basin to the North where the Mount Simon sandstone is exploited as a water resource ?
4. Will CO_2 injection result in significant vertical brine displacement across the Eau Claire confining unit?

5. Are there optimal regions of the basin that would likely minimize pore pressure generation and the potential for induced seismic activity?

As noted by the ground breaking study of Birkholzer et al. (2007), some of these questions need to be addressed at the sedimentary basin-scale to ensure that unforeseen well-well interactions do not occur while others can be addressed with more localized analysis. We argue below that there are alternatives to using computationally expensive, multi-phase simulators to address these issues at the sedimentary basin scale. Recently, Nordbotten et al. (2004, 2005) argued that simple, analytical models based on sharp-interface theory are of great value in providing order of magnitude estimates of the hydrologic and environmental consequences of CO_2 injection. By using sharp-interface theory, these authors were able to capture much of the relevant physics of the CO_2 injection problem without relying on numerical methods. In this study, we addressed the questions presented above by developing sharp-interface models of CO_2 injection across the Illinois basin. Our calculations are compared to multi-phase models including TOUGH2 (Birkholzer et al. 2007). Our study does not consider the effects of CO_2 leakage along abandoned petroleum wells (Nordbotten et al.; 2004, 2005). We also compare our model results and those of Birkholzer et al. (2007) to single phase analytical solutions of Hantush and Jacob (1955).

2. Study Area

The Illinois Basin is an intercratonic Paleozoic basin which formed in response to thermal subsidence and Appalachian tectonics (Kolata and Nelson, 1990; Beaumont et al., 1988). It is slightly elongated in a NW-SE direction (Fig. 4). It is about ~620 km long, 375 km wide, and over 4.5 km in depth. Our analysis focuses on the basal Cambrian Mount Simon Sandstone reservoir and overlying Eau Claire confining unit which overlies the Precambrian basement (Lloyd and Lykes, 1995). The slope on the Mount Simon is low (0.006; Fig. 5). Mount Simon thickness varies from 50 to 610 m from North to South (Fig. 6). Medina et al. (2008) subdivided the Mount Simon Sandstone into three subunits based primary on the gamma ray response from borehole geophysical logs (Fig. 7). A generalization of the

178 subunits is as follows: the upper unit has a relatively high value of gamma ray possibly due the
179 admixture of more argillaceous material resulting from the transition from a high energy, open marine
180 settings to a quieter more clay-rich depositional environment. The middle unit was defined by its
181 lower gamma ray values that result from a cleaner sandstone and probably constitutes the main flow
182 unit, whereas the lowermost unit was defined by gamma ray values that progressively increases with
183 depth to the base of the formation. This increase is due to the increased non-quartz fractions in the
184 formation as the top of the Precambrian basement complex is approached. In this study, we focused on
185 CO_2 injection into the middle unit of the Mount Simon. The Eau Claire Formation, a unit that is
186 dominantly shale, functions as a confining unit over the Mount Simon (Gray stippled pattern, Fig. 7).
187 The Eau Claire thickness varies between 50-100m. Permeability data on the Eau Claire is not plentiful
188 and there is considerable uncertainty in how it changes with depth and with scale (Birkholzer et al.
189 2007). The few available permeability measurements of Eau Claire permeability range between 1.4 x
190 10^{-18} to 6.7 x 10^{-20} m^2 (0.002 – 0.00067 mD) as reported by Witherspoon et al. (1962), Walton (1962),
191 and Witherspoon and Neuman (1967). Birkholzer et al. (2007) argued that the presence of fractures
192 could increase the effective basin scale vertical permeability of the Eau Claire by about two orders of
193 magnitude. These two units are overlain by a sequence of Ordovician to Pennsylvanian–age
194 sandstones, shales, and carbonate and coal units (Fig. 4). A thin veneer of Pleistocene to Quaternary-
195 age unconsolidated sediments overlies the basin, along the northern glaciated margin, in stream
196 valleys, and the Mississippian Embayment to the south. The surface topography of the basin is
197 relatively subdued, with less than 300 m of relief. The southern margin of the Illinois Basin was
198 deformed during the late Paleozoic through Mesozoic by tectonic uplift of the Pascola Arch and
199 downwarping of the Mississippian Embayment. Uplift was accommodated, in part, by the generation
200 of the Cottage Grove and Rough Creek-Shawneetown fault systems which trend east-west and extends
201 from the Precambrian basement to the surface (Fig. 4). The Wabash Valley fault system was also
202 rejuvenated at this time.
203

Four prior basin-scale hydrogeologic models within the Illinois Basin have been developed by Bethke et al. (1991), Gupta and Bair (1997), and Breemer et al. (2002), and Birkholzer et al. (2007). The study of Gupta and Bair (1997) presented drill-stem test (DST) data suggesting hydraulic heads within the Mount Simon were near hydrostatic levels (Fig. 8A). Elevated freshwater heads vary from about 200 to -50 meters above sea level (Fig. 8A). Head gradients across the Mount Simon are rather low (0.0003). Within the water table aquifer across the Illinois Basin (not shown), flow is generally from the north to south but with significant local flow systems associated with surface water drainage networks. The Mount Simon formation across the Illinois basin is characterized by lateral high salinity gradients (Fig. 8B-C; Hanor, 1987; McIntosh and Hanor, 2006). Bethke et al. (1991) argued that brines and hydrocarbons migrated through the Illinois Basin over relatively long geologic time scales (millions of years) and over 600 km distance, driven by tectonic uplift of the Ouachitas and Pascola Arch. It is also likely that Pleistocene glaciations have influenced salinity patterns across the Illinois Basin (McIntosh et al. 2004; Schlegel et al. 2008). The Illinois Basin was over run by the Laurentide ice sheets at least twice during the late Pleistocene (see orange solid and dashed lines, Fig 4). Breemer et al. (2002) developed a series of NE-SW cross-sectional hydrologic models across the Illinois basin following the traverse of the Lake Michigan Lobe of the Laurentide Ice Sheet. The goal of this study was to assess the development basal pore pressures conditions beneath the ice sheet to better understand sliding and basal sediment deformation mechanisms beneath this ice lobe. Their results suggest that the asymmetric salinity pattern from north to south may have been caused by ice sheet derived infiltration (Person et al. 2007). Stable isotope composition and Na-Ca-Cl-Br relations of formation waters within the Illinois basin are indicative of evapo-concentrated seawater, suggesting that these Paleozoic-age fluids are relatively stagnant and have not been flushed by meteoric recharge (Stueber and Walter, 1994). Membrane filtration has also been proposed as a mechanism for high brine concentrations within the Illinois Basin (Bredehoeft et al. 1963) although this has not been confirmed by stable isotope data.

Birkholzer et al. (2007) presented models evaluating the basin-scale consequences of CO_2 injection across the Illinois Basin (Figure 9) using a parallel version of TOUGH2. Like this study, these authors considered CO_2 injection into the Mount Simon and overlying Eau Claire confining unit. CO_2 was injected into 26 wells located in the center of the Illinois Basin in south central Illinois and Indiana (Fig. 9). These authors varied the rate of CO_2 injection between 5-15 million metric tons/year/well ($2.7 - 8.2 \cdot 10^4$ m^3/day assuming a CO_2 density of 500 kg/m^3). They assigned a permeability to the Eau Claire of 10^{-18} m^2. The permeability of the member of the Mount Simon that received CO_2 was set to 1000 mD. The water saturated aquifer compressibility was assigned of about $7.0 \cdot 10^{-10}$ Pa^{-1} based on a long-term pump test results (S~0.3). The total thickness of the Mount Simon that received CO_2 was about 95m. Owing to the high permeability of the Mt Simon (1 darcy) computed pressures propagated across the entire Illinois Basin (> 200 km) after 30 years of continuous injection (Fig. 9A). Pore pressures never exceeded 3 MPa owing to the relatively permeable conditions represented in their model. The separate phase CO_2 plume was confined to a narrow region around the injection well (about 3 km radial distance).

Cores from the Mount Simon sandstone (Cambrian) and its lateral equivalents in Ohio, Michigan, Kentucky, West Virginia, Pennsylvanian and New York were analyzed as part of the Midwest Regional Carbon Sequestration Partnership (MRCSP) (Medina et al. 2008). Porosity data obtained from 128 core analyses and inferred from 189 geophysical logs suggest that pore volume decreases with depth from 0.27 to 0.02 following an Athy-type (Athy, 1930) relationship due to mechanical compaction and diagenetic changes (Figure 10). Medina et al. (2008) used the data presented in Figure 10 to develop a best fit relationship between porosity-depth. Medina et al. (2008) also presented results from a total of 2,472 permeameter tests performed on core samples from Indiana (1,875 data points), Michigan (458 data points), Ohio (131 data points), and Kentucky (8 data points) indicate a log-linear positive relationship between porosity and permeability (Figure 11). Permeability varies between 10,000 to 0.01 mD within the Mount Simon. The average Mount Simon permeability is about 60 mD.

3. Methods

3.1 Analytic Single-Phase Models

Our analysis of the Mount Simon aquifer and Eau Claire confining unit begins by developing simple analytical models of CO_2 injection into a homogenous, isotropic aquifer overlain by a leaky confining unit following the approach of Hantush and Jacob (1955). The approach is idealized because it assumes a single fluid phase under conditions of steady-state leakage across a confining unit. Our single phase assumption is justified by the observation that the CO_2 phase is restricted to a narrow region around the injection well as demonstrated by Birkholzer et al., (2007). The Eau Claire is assigned a constant thickness and permeability. The governing equation describing radial flow under conditions of single phase fluid injection and leakage across an overlying confining unit is given by (Hantush and Jacob, 1955):

$$\frac{S}{T}\frac{\partial s}{\partial t} = \frac{1}{r}\frac{\partial s}{\partial r} + \frac{\partial^2 s}{\partial r^2} - \frac{K'}{Tb'}s \qquad (1)$$

where S is the storativity, r is radial distance from the injection well, t is time, s is change in head above hydrostatic, T is aquifer transmissivity, K' in the hydraulic conductivity of the confining unit, and b' is the thickness of the confining unit. These authors solved equation (1) subject to the following boundary conditions:

$$s\left(r=\infty, t\right) = 0$$
$$r\frac{\partial s}{\partial r} = -\frac{Q}{2\pi T} \qquad \lim r \to 0 \qquad (2)$$

where Q is the volumetric CO_2 injection rate. We assume hydrostatic initial conditions (i.e. s(r, t=0) = 0 m). Hantush and Jacob (1955) found that the solution to equation (1) is given by:

$$s = \frac{Q}{4\pi T} L(u,v) \quad (3)$$

where

$$u = \frac{r^2 S}{4Tt} \qquad v = \frac{r}{\beta} \qquad \beta = \sqrt{T \frac{b'}{K'}} \quad (4)$$

Values of the function L(u, v) are provided by Walton (1960). We assigned transmissivity, saturated thickness, and leakance values assuming a water saturated phase. We hypothesize that water will be the dominant phase away from the injection well where there is abundant opportunities for leakage. However, we assigned the storage coefficient based on compressibility of the CO_2 phase.

3.2 Sharp-Interface Model

As outlined by Nordbotten et al. (2005, 2008) and demonstrated by Birkholzer et al., (2007) CO_2 injection will result in a largely water wet system with regions of high CO_2 saturation confined to relatively small regions near the injection well annulus. While the sharp interface approach uses only end-point values of relative permeability and phase saturation, detailed comparisons between sharp-interface and multi-phase codes have shown excellent agreement between computed and observed pore pressures and CO_2 plume geometry when common petrophysical parameters are used (Gasda et al. 2008). The main limitation of the sharp-interface approach is its inability to represent the initial dynamics of vertical segregation of phases within a formation, and the limited representation of inter-formational vertical heterogeneity through expressions for effective relative permeability that result from vertical averaging. Recently, sharp-interface theory has been used to quantify the potential of CO_2 leakage along abandoned oil and gas wells within sedimentary Basins (Nordbotten et al., 2004, 2005). These authors developed analytical solutions based on sharp-interface equations to quantify reservoir injection pressures and supercritical CO_2 lens thickness within a homogenous, isotropic reservoir as well as determine CO_2 loses associated from an adjacent leaky well bore. Because well

306 density can be quite high in some reservoirs, these authors argued that numerical solutions are
307 impractical. Following Gasda (2008), we have extended the approach of Nordbotten et al. (2004) by
308 developing numerically based on sharp-interface models of CO_2 injection. The rational for developing
309 a numerical sharp-interface model is to represent the effects of spatial variations in
310 permeability/porosity associated with burial depth and facies heterogeneity within the Mount Simon
311 sandstone.
312
313 The governing equations describing CO_2 injection into a leaky, confined aquifer within a sedimentary
314 basin using sharp-interface theory we used here are similar to the methodology outlined by Ledoux et
315 al. (1990). This approach has also been applied to two-phase petroleum systems (Lehner et al., 1987;
316 Rhea et al., 1994). We invoke some restrictive simplifying assumptions in applying sharp-interface
317 theory to the CO_2–brine transport problem. First we assume that the top of the reservoir or carrier bed
318 is flat with an elevation of zero. The CO_2 heads are initially set to zero (i.e. no regional head gradients
319 are imposed). Elevated CO_2 heads are due solely to the effects of supercritical injection (Fig. 12). We
320 will address the effects of buoyancy and hydrodynamic driven flow within the Mount Simon
321 Sandstone on long-range, separate-phase CO_2 migration later using an approach first presented by
322 Hubbert (1953) described below. Gasda's (2008) sharp-interface model has overcome these
323 simplifying assumptions using sharp-interface theory.
324
325 In our sharp-interface approach, two, transmissivity-based flow equations describing changes in
326 freshwater head (h_f) as well as the position of the CO_2-brine (z_{ic}) interface are solved (Fig. 12):
327
328 *CO_2 Transport:*

329 $$\left(z_t - z_{ic}\right)S_c \frac{\partial h_c}{\partial t} - \phi\left(1 - S_r\right)\frac{\partial z_{ic}}{\partial t} = \frac{\partial}{\partial x}\left[T_c \frac{\rho_f}{\rho_c}\frac{\partial h_c}{\partial x}\right] + \frac{\partial}{\partial y}\left[T_c \frac{\rho_f}{\rho_c}\frac{\partial h_c}{\partial y}\right] + q_c \qquad (5)$$

330
331

Brine Transport:

$$\phi\left(1-S_r\right)\left[\frac{\partial z_{ic}}{\partial t}\right]=\frac{\partial}{\partial x}\left[T_s\frac{\rho_c}{\rho_s}\frac{\partial h_c}{\partial x}+T_s\left(\frac{\rho_s-\rho_c}{\rho_c}\right)\frac{\partial z_{ic}}{\partial x}\right] + \frac{\partial}{\partial y}\left[T_s\frac{\rho_c}{\rho_s}\frac{\partial h_c}{\partial y}+T_s\left(\frac{\rho_s-\rho_c}{\rho_c}\right)\frac{\partial z_{ic}}{\partial y}\right]-q_l \quad (6)$$

where

h_c – CO_2 heads
z_{ic} – brine - CO_2 interface
z_t – elevation of the top of the reservoir
φ – porosity
q_c – injection rate of CO_2 into aquifer
q_l – aquifer leakance across a confining bed
S_r – residual water saturation
Ss - brine specific storage (Ss ~ ρ_s g β)
β – reservoir compressibility
ρ_c – density of CO_2
ρ_s – density of brine phase

Our sharp-interface approach assumes brine and supercritical CO_2 flow occurs only in the horizontal direction. While CO_2 density changes considerably with pressure and temperature (Nordbotten et al. 2005), our model assumed that fluid properties were spatially invariant. Our analysis considers changes in CO_2 storage due to changes in saturation and compressibility effects although the later is relatively small in comparison. Our analysis neglects diffusion of CO_2 into the brine phase (Lu and Lichtner, 2007) and fluid-rock geochemical reactions which may be significant on geologic time scales.

The head of CO_2 presented in equations (5-6) is given by:

$$h_c=\frac{P}{\rho_c g}+z \quad (7)$$

where

P – CO_2 fluid pressure
g – gravity constant

z – elevation

The head of the brine phase (h_s) is explicitly related to the head of CO_2 as follows:

$$h_s = \frac{\rho_c}{\rho_s} h_c + \frac{\rho_s - \rho_c}{\rho_s} z_{ic} \quad (8)$$

Due to the assumed coarse grain sized of the reservoir rocks, capillary forces are neglected in equations (7-8). We calculate the rate of brine leakance across the Eau Claire using a one-dimensional expression of Darcy's Law:

$$q_l = -\frac{K_z}{b'}\left(h_s - h_o\right) \quad (9)$$

where

K_z – vertical hydraulic conductivity of the brine phase within the confining unit
h_o – is the head above the confining unit
h_s – is (complete)
b' is the thickness of the confining unit

Our approach also neglects transient storage changes on flow within the confining unit. If the CO_2 lens thickness at the top of the reservoir exceeds 1 m, we reduce the vertical hydraulic conductivity of the confining unit by three orders of magnitude to minimize leakage in regions where CO_2 is present at the top of the reservoir. We do not consider separate phase CO_2 migration across the Eau Claire Formation. The transmissivities for the CO_2 and brine phases is defined as:

$$\begin{aligned} T_c &= K_c\left[z_T - z_{ic}\right] \\ T_s &= K_s\left[z_{ic} - z_b\right] \end{aligned} \quad (10)$$

where

K_s and K_c – vertically-averaged saturated hydraulic conductivities of the brine and CO_2 fluid phases ($K_i = k\rho_i g/\mu_i$; where *i* refers to the respective fluid phase;
T_c and T_s - transmissivities for the CO_2 and brine phases.
z_{ic} – CO_2-brine interface
z_T – top of aquifer
z_b – base of aquifer

If the computed interface falls below the bottom of the reservoir, a maximum saturated thickness based on the total formation thickness is assigned in determining the reservoir transmissivity. We reduced the porosity by a factor of 100 in elements where the interface reached the bottom of the Mount Simon to minimize mass balance errors and promote lateral spreading of the CO2-brine interface (Ledoux et al. 1990). We also maintain a minimum saturated thickness for each fluid phase (5% of total thickness) to permit the lateral movement of pressure and the CO_2 phase.

Equations 5-6 provide an accurate estimate of heads and interface near the injection wells where the CO_2 lens is non-zero. However, they don't provide an accurate prediction of far-field brine heads (h_s) because the CO_2 phase is zero away from the injection well. To overcome this limitation, we adopted the approach of Gasda (2008) and also solve a single, transmissivity based flow equation for brine head (h_s) summing CO_2 and brine transmissivity and storativity:

$$\frac{\partial}{\partial x}\left[(T_s + T_c)\frac{\partial h_s}{\partial x}\right] + \frac{\partial}{\partial y}\left[(T_s + T_c)\frac{\partial h_s}{\partial y}\right] = \left[(z_t - z_{ic})S_c + (z_{ic} - z_b)S_s\right]\frac{\partial h_s}{\partial t} \qquad (11)$$

where

S_s – brine specific storage coefficient

The saturated thickness of the CO_2 phase is defined by the elevations of the sharp-interface position and reservoir thickness.

417 **3.3 Numerical Methods**

418 We solved the above system of equations (5-6, 11) using the finite element method (Taylor and
419 Person, 1996, Person et al. 1998). We solved equations 5-6 simultaneously given that there are two
420 unknowns in each equation (h_c, z_{ic}). Equation 11 was solved separately using the freshwater and CO_2
421 lens thicknesses computed in equations 5-6. We solved the two sharp interface equations (5-6)
422 simultaneously using Gaussian elimination. We then solved for brine head in equation 11 using the
423 saturated thickness determined from equations 5 and 6. We validated our model using
424 PFLOTRAN/FEHM for a single well injection as described below.

425

426 **3.4 Boundary and Initial Conditions**

427 For the basin scale model we specified a constant head and CO_2 lens thickness of zero along the
428 northern edge of our solution domain. All other boundaries were no flow. For intermediate scale
429 models, the same boundary and initial conditions were enforced.

430

431 **3.5 Hubbert CO_2 Potential**

432 The simplifying assumptions described above prevent us from computing the long-range migration
433 pathways CO_2 due to buoyancy and hydrodynamic effects. We quantified long-range separate-phase
434 CO_2 migration away from injection wells due to buoyancy (i.e. bed slope) and due to regional
435 groundwater flow patterns using the approach of Hubbert (1953). Hubbert's oil potential has been
436 used to assess the relative effects of groundwater flow on petroleum migration and entrapment in a
437 number of petroleum basins around the world including the Williston Basin (Berg et al. 1994),
438 Alberta Basin (Bekele et al. 2002), Illinois Basin (Bethke et al. 1991), and Paris Basins (Bekele et al.
439 1997). Following Hubbert's approach, we assume here that buoyancy driven supercritical CO_2
440 migration within porous, permeable reservoir rocks, is controlled primarily by the slope of the top of
441 the reservoir as well as the density contrast between supercritical CO_2 and formation waters:

442

443 $$\eta_C = \frac{\rho_w}{\rho_C} Z_{ls} - \frac{\rho_w - \rho_C}{\rho_C} z_t \quad (12)$$

444

445 where η_c is Hubbert's CO_2 heads, h is hydraulic head within the Mount Simon, ρ_s is brine density, ρ_C
446 is oil density, z_t is the elevation of the top of the reservoir. We explicitly computed the lateral CO_2
447 migration rates as follows:

448

449 $$q_x = -\frac{K_C}{\phi}\frac{\partial \eta_c}{\partial x}$$
$$q_y = -\frac{K_C}{\phi}\frac{\partial \eta_c}{\partial y} \quad (13)$$

450

451 where K_c is the CO_2 conductivity and q_x, and q_y are the components of CO_2 velocities in the x- and y-
452 directions. We used the velocity field from equation (15) to produce particle streak lines of long-range
453 CO_2 migration across the Illinois Basin.

454

455 **3.6 Model Verification**

456 We attempted to verify in part, our sharp-interface model, in part, by attempting to reproduce a simple
457 a numerical injection experiment carried out using PFLOTRAN (Lu and Lichtner, 2007) and FEHM
458 (Pawar, 2007). These codes include equations of state for CO_2 and brine phases, relative permeability,
459 and residual saturation effects. Supercritical CO_2 was injected into a reservoir at a rate of 2.3 kg/s (370
460 m^3/day assuming a density of 748 kg/m^3) for a period of ten years. The hydrostatic pressure at the top
461 of the 63 meter thick reservoir was set as 20 MPa (depth of 2 km). No vertical leakage was permitted.
462 The PFLOTRAN and FEHM solutions domain extended 1000 m away for the injection well. The
463 PFLOTRAN/FEHM grid had a constant vertical cell dimension of 2 meters and used 32 rows of
464 elements. It employed a uniform grid with a lateral dimension of 2 m (i.e. Cartesian grid). The
465 permeability and porosity of the reservoir was set at 10 mD (10^{-14} m^2) and 0.15, respectively. We used

466 a telescoping finite element grid consisting of 2,847 nodes with a cell size varying from 5 m to 30 m.
467 We used a water and CO_2 viscosity of 0.001 and 0.00007 Pa-s, respectively.
468
469 PFLOTRAN/FEHM computed pressures (Fig. 13B) had to be vertically averaged and converted to
470 CO_2 heads to compare to Sharp-CO_2 (Fig. 13D). The CO_2-brine interface was inferred to be located
471 near the 0.5 CO_2 saturation (Fig. 13A). Near the well bore, the maximum excess head computed by
472 PFLOTRAN was about 150 m while the CO_2 head from our sharp-interface model was about 230 m.
473 Both codes predicted a linear variation in head out beyond the region of CO_2 saturation (Fig. 13D).
474 The computed position of the CO_2-brine interface in all the three models, compared favorably. The
475 CO_2 lens was restricted to the narrow region around the well and the pressure pulse propagated out
476 much further.
477
478 **4. Results**
479 **4.1 Single-Phase Analytic Injection Models**
480 We begin our analysis with the analytical solution of Hantush and Jacob (1955) presented in Section
481 3.1. We assigned a storage value (0.05) based on the compressibility of CO_2. Supercritical CO_2
482 compressibility (e.g. 1.43E-07 Pa^{-1} at 38 ^oC and 1064 m depth) is several orders of magnitude higher
483 than water compressibility (4.5E-10 Pa^{-1}) but is on the same order of magnitude of sediment
484 compressibility of unconsolidated sands (Freeze and Cherry, 1979). Since there is significant
485 uncertainty in the permeability of the Mount Simon aquifer and Eau Claire confining units we varied
486 their values between 5-125 mD and 0.0001-0.01 mD, respectively (Table 1). The pumping rate we
487 used is the same as is used later in our basin scale sharp-interface models.
488
489 We used a CO_2 injection rate of 10^5 m^3/year. Run 1 represents what we consider the most typical
490 parameters for the Mount Simon (50 mD) and Eau Claire (0.001 mD) confining unit (Fig. 14A). The
491 computed peak deviatoric pressure was about 2.5MPa (Fig. 14A). The leading edge of the pressure
492 disturbance propagated out to about 18 km after 100 years of continuous injection. The rate of

advance of the CO_2 pressure front decreased through time from 130 m/year after 10 years of injection to about 60 m/year after 100 years. Lowering the permeability of the Eau Claire by one order of magnitude (0.0001 mD; Run 2, Table 1; Fig. 14B) and increasing the Mount Simon permeability by to 125 mD pushed the leading edge of the pressure disturbance out to about 20 km after 70 years. Deviatoric pressures within the Mount Simon aquifer increased to about 18 MPa. Lowering the permeability of the Mount Simon to 5 mD and increasing the permeability of the Eau Claire to 0.01 mD (Run 3, Table 1; Fig. 14C) resulted in the highest heads (25 MPa) but yielded the smallest radius of pressure disturbance (about 6 km after 100 years of continuous injection). Unlike the study of Birkholzer et al. (2007) these analytical solutions suggest that CO_2 injection within the Mount Simon will result in a finite radius of pressure disturbance from the injection point, which in most cases will be contained within a well field, on the order of about 20 km. If other wells are located within a radial distance of 6-20 km, there will be significant well-well interference. At a depth of 1.5 km, the excess pressure generated by our analysis was about 50% of the lithostatic pressure. Using the parameters and injection rates (2.75×10^4 m3/year) of Birkholzer et al. (2007) (Fig. 14D), produced a pressure envelop on the order of 200km and a pressure anomaly at the well head of 2.2 MPa. These values are closer to what their TOUGH2 model predicted (3 MPa or 30 Bars).

Intermediate- to Basin-Scale Sharp-Interface Models of Illinois Basin

We constructed one basin-scale (Figure 15A) and two intermediate-scale (Figures 15B-C), finite-element models of the Mount Simon-Eau Claire reservoir-confining unit across much of the Illinois Basin using the sharp-interface approach. The basin scale model domain is wedge shaped with a length of 600 km to the northwest direction and has a width which varied between 260 to 510 km in the southeast-northwest direction (Fig. 15A). Fluid and rock properties used in our model are listed in Table 2. To the south, the basin-scale model terminates near the Rough Creek Fault System at the margin of the basin where the reservoir becomes deep and thin as to be less effectual. To the north, the model terminates about 50 km south of Chicago where the groundwater within pore spaces of the Mount Simon is still saline (>50,000 ppm TDS). The two intermediate (64 by 47 km and 50 by 70

520 km) models (Fig. 15B-C) were also constructed to study well-well interference patterns and CO_2 lens
521 geometry at a higher spatial resolution. The basin-scale finite element mesh is comprised of 8,160
522 nodes and 16,122 elements (Fig. 15A). The two intermediate scale grids were composed of between
523 8,081 and 9,077 nodes and 16,058 and 18,042 elements (Fig. 15B-C). The intermediate scale models
524 are located in the middle and deep sections of the Illinois basin. This was done to evaluate the impacts
525 of permeability and porosity trends with depth on computed excess pressures and CO_2-brine interface
526 positions using a more highly resolved grid.
527
528 We allowed thickness, permeability, and porosity to vary spatially across the basin (Fig. 1B). The Eau
529 Claire confining unit varies in thickness from north to south from 61 to 152m.
530 We allowed the Mount Simon reservoir permeability to decrease in a linear fashion from 125 mD to
531 10 mD from north to south. Porosity also decreases from 15% to 5% from north to south. The
532 thickness and elevation of the Mount Simon sandstone varies from north to south from less than 150
533 to 610 m (Fig. 6). The maximum thickness of the Mount Simon occurs near the northern edge of the
534 Illinois Basin (Fig. 6).
535
536 **4.2 Sharp-Interface Model Results**
537 We represented the effects of CO_2 injection from 42 power plants in our model using 726 injection
538 wells. These wells were spaced in radial patterns between 2-4 km from the power plant sites (Fig.1C).
539 Some wells were removed if they were located within 1 km of another injection well from an adjacent
540 power plant. Preliminary models that used between 1-12 injection wells per power plant to emplace
541 the 80 million metric tons of CO_2 per year resulted in simulated pore pressures that exceeded
542 lithostatic pressures in some locations.

543 We injected continuously for a period of 100 years. We then shut the wells in for 100 years to
544 determine the long-term fate of pore pressures and CO_2 lens position. Computed deviatoric pressures
545 after 100 years were highest (up to 16.4 MPa in Fig. 16A, 17A) in the deepest part of the basin where

546 permeability is lowest (about 5 mD). In the middle of the basin at intermediate depths (permeability
547 about 50mD), excess pressures reached only about 4.4 MPa (Fig 16A, 17C) after 100 years. The
548 maximum radial distance of pressure disturbance (>0.03 MPa or 3m of freshwater head) away from
549 individual injection wells was on the order of 9-13 km across the basin. The wells were shut in after
550 100 years of injection. After 200 years (100 years of shutin) fluid pressures dissipated and the region
551 of pressure disturbance increased out to radial distances of about 15-30 km (Figs. 16B, 17B and 17D).
552 Maximum fluid pressures decreased to between 3.6 to 9.8 MPa at intermediate and deep portions of
553 the Illinois Basin. The net diameter of the pressure disturbance envelop around the injection well
554 centers was about 50 km and there is significant well-well pressure disturbance between adjacent
555 injection well centers. Intermediate scale simulations provide higher resolution images of pressure
556 disturbance patterns. After 100 years of shutin it is difficult to see the positions of individual wells at
557 all depths (Fig. 17B, D). However, note that the pressures will never return to hydrostatic conditions
558 due to buoyancy effects.

559

560 The thickness and geometry of the computed CO_2 lens shows important differences across the basin
561 (Fig. 18). Because the Mount Simon is thinnest (only 50m thick) and of low porosity (0.05) in the
562 deepest, southern most part of the basin, the CO_2-brine interface reaches the base of the formation
563 before displacing brines laterally (Fig. 18a). At intermediate depths, the CO_2 lens doesn't reach the
564 base of the Mount Simon and attains a maximum thickness of 60 m. At intermediate depths, it spreads
565 further laterally due to the increased Mount Simon permeability and porosity (Fig. 18C). The radius
566 of the CO_2 plume varies between the deep and intermediate parts of the basin between about 0.5-2.0
567 km depending on local porosity levels. There is little well-well interference between individual CO_2
568 lenses after 100 years. After 100 years of shutin, the CO_2 lens has spread considerably at intermediate
569 depths (Fig. 18D). The CO_2 lens lateral migration is much less in the deepest part of the basin (Fig.
570 18B). The maximum thickness of the CO_2 lens at intermediate depth is only 12 m after 100 years of

shutin. The CO_2 lens footprint is still much smaller when compared to the region pressure disturbance (compare Figures 17 and 18 after 100 years of shutin).

Simulated vertical leakage of brines across the Eau Claire confining units was highest (10^{-5} m/day; Fig 19C-D) around the injection wells just beyond the CO_2 lens terminates and dissipated quickly. After 100 years brines would have moved about 0.5 meters into the Eau Claire formation. Brine displacement was negligible at a radial distance of about 5 km from an injection well (Fig. 19A). This is due, in part, to leakage represented across the Eau Claire confining unit. Our analysis suggests there will be very limited brine displacement at the basin-scale.

To assess the potential that CO_2 injection could induce earthquakes, we plotted pore pressure verses depth for the two intermediate scale models. These show that pore pressures exceed hydrostatic pressures in the deepest part of the basin (Figure 20) but are close to hydrostatic at intermediate depths. Fluid pressures reach 46% of lithostatic pressure between 3000-3500 m depth. We also plotted pore pressures generated at the two hazardous waste injection wells near Lake Erie reported by Nicholson and Wesson, (1988, 11 MPa, open circle). This value is far below lithostatic levels.

One potential effect of increased fluid pressures is uplift of the land surface. We estimated the amount of uplift within the Mount Simon by using the following relation:

$$\Delta L = b \Delta P \alpha_{ul} \qquad (15)$$

where ΔL is the amount of uplift (m), ΔP is the deviatoric pore pressure (Pa), b is the local thickness of the Mount Simon formation (m) and α_{ul} is the unloading compressibility. The compressibility (8.0×10^{-9} Pa^{-1}) we used is relatively low for sandstones (Freeze and Cherry, 1979) and is intended to represent unloading conditions (Corbet and Bethke, 1992). We used pore pressures presented in Figure 16 to compute uplift. Local Mount Simon thickness was used. Results indicate that up to 6 m

598 of uplift would occur assuming the unloading compressibility used (Figure 21). The magnitude of
599 uplift was similar for the intermediate and deep portions of the basin due to the offsetting effect of
600 decreasing Mount Simon formation thickness with increasing pore pressure to the south.
601
602 **4.3 Long-Range CO_2 Migration Due to Buoyancy and Hydrodynamic Drives**
603 Our sharp-interface models were unable to represent the effects of long-range separate phase CO_2
604 migration because of the underlying assumptions described above (i.e. a constant elevation assigned to
605 the Mount Simon Formation and no regional head gradients). However, using Hubbert (1953)
606 (equations 12-13) potential theory, we were able to estimate the rate of separate phase CO_2 migration.
607 We found that separate phase migration would be induced primarily due to the effects of buoyancy
608 (bed slope). The buoyant drive is low due to the gentle slope on the Mount Simon from North to South
609 (about 0.008 m/m). However the hydrodynamic drive is even less due to the low hydraulic gradients
610 within the Mount Simon (Fig. 8A; about 0.0008 m/m). Our analysis suggests that separate phase CO_2
611 within the deepest portion of the basin would migrate up gradient to the north before becoming
612 entrapped within gentle structures in the middle of the basin (Fig. 21). The migration rates are small (6
613 m/1000 years) and it is likely that much of the CO_2 would either diffuse into the water phase, be
614 trapped in the capillary pore spaces, or become fixed in the reservoir as a solid mineral phase on these
615 time scales (Rubin et al., 2005).
616
617 **5. Discussion and Conclusions**
618 We had originally suspected that the injection of 80 million metric tons of CO_2 per year over a period
619 of 100 years at 41 sites would lead to significant displacement of brines towards the margins of the
620 basin and basin scale pressure anomalies. However, because of leakage of brine across the Eau Claire
621 confining unit and the distributed nature of power plant locations across the States of Illinois and
622 Indiana, our models indicated that long-range (> 20 km) lateral movement of brines and pressure
623 anomalies will not develop. That said, the model predicts that pressures in excess of 16.4 MPa would
624 occur in the deepest parts of the basin and pressure interference patterns would emerge between

adjacent injection wells in the more permeable center of the basin. Our calculated maximum pressure anomaly was about 5 times higher than that predicted by simulations using TOUGH2 (Birkholzer et al. 2007; 3 MPa). However, our computed pressure anomalies were restricted to a distance of about 13 km from injection wells in our sharp-interface models. Since the analytical results presented in Figure 14, were able to nearly match Birkholzer et al. 2007 and our sharp interface results, we suspect that these differences are mostly due to the differences in selection of petrophysical parameters (1000 mD for Birkholzer et al. 2007 verses 125 mD for this study) rather than differences in model assumptions. One of the biggest surprises of our study is how well simple analytic solutions can approximate the results of more complex multiphase simulations.

Significant anomalous pressures due to CO_2 injection only developed in the deepest part of the Illinois Basin where the permeability is lowest (Fig. 16D). While excess pressures were about 46 % of the lithostatic load, they would have been much higher if fewer wells had been used. Relatively low deviatoric pressure conditions to the north suggest that the middle portion of the Illinois Basin is probably the best venue for injection. This is especially true if one considers seismic hazards which are concentrated to the south. If CO_2 transmission costs are not prohibitive, then power utilities should consider focusing on the middle of the Illinois Basin for long-term injection programs.

Long range CO_2 migration by buoyancy or hydrodynamics does not appear to be an important concern. Salinity changes induced by brine migration into low porosity confining units are capable of producing significant osmotic pressures up to 20 MPa (Neuzil, 2000) if significant concentration gradients develop. This could lead to unanticipated consequences such as hydrofracturing. While vertical brine leakage rates are low, the presence of abandon wells may still be a factor (Nordbotten et al. 2004, 2005) in CO_2 leakage. If CO_2 remains in a separate phase over geologic time scales, buoyancy effects would cause it to travel at a rate of 6 m/1000 years to the north. The effects of groundwater flow on CO_2 migration are small due to the gentle head gradients.

Our basin-scale model was able to represent 200 years of CO_2 injection, migration, and pore pressure development at the sedimentary basin scale using serial computer. Equivalent two-phase simulations representing 30 years of injection required the use of high performance computing. While our sharp interface model is relatively simple (e.g. we only consider one reservoir and one confining unit), it could be used to perform first cut assessments of optimal location and type (horizontal verse vertical) of CO_2 injection wells across the Illinois Basin. It serves as an end member, a worst case scenario, in the set of linked analyses that must ultimately consider the effects of dissolution into the brine, capillary entrapment and mineral precipitation in the overall performance of fluid migration in a basin. If a system of pure piston-like displacement has such minimal effects on pressure and brine migration, when other mitigating factors as itemized above are integrated, the migration scenarios should be even less distinct. More work could also be done in the Illinois Basin extending our analysis to multiple formation targets for CO_2 injection (e.g. the Knox carbonate section, New Albany Shale and Pennsylvanian coals) and calibrating our model to match available pressure (Gupta and Bair, 1999) and salinity data. This would involve linking multiple sharp-interface reservoirs/confining unit models together at the basin scale.

668 **6. References**

669 Athy, L.F., 1930. Density, porosity, and compaction of sedimentary rocks. American Association of
670 Petroleum Geologists Bulletin. 14, 1-23.
671 Beaumont, C., Quinlan, G., Hamilton, J., 1988. Orogeny and stratigraphy: numerical models of the
672 Paleozoic in the eastern interior of North America. Tectonics. 7, 389-416.
673 Bethke, C.M., Reed, J.D., Oltz, D.F., 1991. Long-range petroleum migration in the Illinois Basin.
674 American Association of Petroleum Geologists Bulletin. 75, 925-945.
675 Berg, R.R., DeMis, W.D., Mitsdarffer, A. R., 1994. Hydrodynamic effects on Mission Canyon
676 (Mississippian) oil accumulations, Bilings Nose area, North Dakota. American Association of
677 Petroleum Geologists Bulletin. 78, 508-518.
678 Beleke, E., Person, M.A., Rostron, B.J., Barnes, R., 2002. Modeling secondary oil migration with
679 core-scale data: Viking Formaion, Alberta Basin. American Association of Petroleum
680 Geologists Bulletin. 86, 55-74.
681 Bekele, E., Person, M., de Marsily, G., 1997. Petroleum migration pathways and charge concentration;
682 a three-dimensional model; discussion. American Association of Petroleum Geologists
683 Bulletin. 83, 1015-1019.
684 Birkholzer, J., Zhou, Q., Zhang, k., Jordan, P., Rutqvist, J., Tsang, C.F., 2007. Large-Scale
685 Hydrological Evaluation and Modeling of the Impact on Groundwater Systems, NETL Project
686 Annual Report, October 1, 2007.
687 Bredehoeft, J.D., Blyth, C.R., White, W.A., Maxey, G.B., 1963. Possible mechanism for concentration
688 of brines in subsurface formations. Bulletin of the American Association of Petroleum
689 Geologists. 47, 257-269.
690 Breemer, C.W., Clark, P.U., Haggerty, R., 2002. Modeling the subglacial hydrology of the late
691 Pleistocene Lake Michigan Loge, Laurentide Ice Sheet. Geological Society of America
692 Bulletin. 114, 665-674.
693 Chadwick, R.A., Zweigel, P., Gregersen, U., Kirby, G.A., Holloway, S., Johannesen, P.N., 2003.
694 Geological characterization of CO_2 storage sites: Lessons from Sleipner, northern North Sea.

Proceedings of the 6th International Conference on Greenhouse Gas Control Technologies (GHGT-6), J. Gale and Y. Kaya (eds.), 1–4 October 2002, Kyoto, Japan, Pergamon, v.I, 321–326

Clauser, C., 1992. Permeability of crystalline rocks. EOS, Transactions American Geophysical Union. 73, 233-240.

Cramer, C.H., Wheeler, R.L., Mueller, C.S., 1992. Analysis for seismic hazard in the southern Illinois Basin. Seismological Research Letters. 73, 792-805.

Corbet, T., Bethke, C.M., 1992. Disequilibrium fluid pressures and groundwater flow in the Western Canada sedimentary basins. Journal of Geophysical Research. 97, 7203-7217.

Eager, K., Pavlis, G., Hamberger, M., 2006. Evidence of Possible Induced Seismicity in the Wabash Valley Seismic Zone from Improved Microearthquake Locations. Bulletin of the Seismological Society of America. 96, 1718–1728.

Freeze, R.A., Cherry, J.A., 1979. Groundwater. 604 pp., Prentice-Hall, New Jersey.

Gasda, S.E., 2008. Numerical Models for Evaluating CO2 Storage in Deep, Saline Aquifers: Leaky Wells and Large-Scale Geological Features, Ph.D. Dissertation, Princeton University.

Gasda, S.E., Nordbotten, J.M., Celia, M.A., 2008. Upslope Plume Migration and Implications for Geological CO2 Sequestration in Deep Saline Aquifers. IES Journal A: Civil and Structural Engineering. 1, 2-16.

Gupta, N., Bair, E.S., 1997. Variable-Density Flow in the Midcontinent Basins and Arches Region of the United States. Water Resources Research. 33, 1785–1802.

Hanor, J. S., Origin and Migration of Subsurface Sedimentary Brines, SEPM Short Course No. 21, 247 pp., Society of Economic Paleontologists and Mineralogists, Tulsa, OK, 1987.

Hanor, J., McIntosh, J.C., 2006. Are secular variations in seawater chemistry reflected in the compositions of basinal brines? Journal of Geochemical Exploration. 89, 153-156.

Hantush, M.S., Jacob, C.E., 1955. Non-steady radial flow in an infinite leaky aquifer: American Geophysical Union Transaction. 36, 95–100.

Hovorka et al., 2001. Evaluation of brine-bearing sands of the Frio Formation, upper Texas Gulf Coast for geological sequestration of CO_2, DOE/NETL-2001/114.

Hsieh, P.A., Bredehoeft, J.D., 1981. A reservoir analysis of the Denver earthquakes; a case of induced seismicity. Journal of Geophysical Research. 86, 903-920.

Hubbert, M.K., 1953. Entrapment of petroleum under hydrodynamic conditions. American Association of Petroleum Geologists Bulletin. 37, 1954–2026.

Kolata, D.R., Nelson, W.J., 1990. Tectonic History of the Illinois Basin, in Leighton, M.W., Kolata, D.R., Oltz, D.F., Eidel, J.J., (editors). Interior Cratonic Basins. American Association of Petroleum Geologists Memoirs. 51, 263 - 285.

Ledoux, E., Rivera, E., and G. de Marsily, 1990. A compatible single-phase/two-phase numerical model, Ground Water. 28, 79-87.

Lehner, F.K., Marsal, D., Hermans, L., Van Kuyk, A., 1987. A model of secondary hydrocarbon migration as a buoyancy-driven separate phase flow, in Migration of Hydrocarbons in Sedimentary Basins, edited by B. Doligez, pp. 457-471, Editions Technip, Paris.

Lindholm, 1990. Effects of present and projected ground-water withdrawals on the Twin Cities aquifer system, Minnesota. US Geological Survey Water Resources Investigation 90-4001, 129 p.

Liu, G., Zheng, C., Gorelick, S.M., 2004. Limits of applicability of the advection-dispersion model in aquifers containing connected high-conductivity channels, Water Resources Research. 40. W08308, doi:10.1029/2003WR002735.

Lloyd, O.B., Jr., Lyke, W.L., 1995. Ground Water Atlas of the United States, Segment 10--Illinois, Indiana, Kentucky, Ohio, and Tennessee: U.S. Geological Survey Hydrologic Investigations Atlas 730-K, 30 p.

Lu, C., Lichtner, P., 2007. High resolution numerical investigation on the effect of convective instability on long term CO_2 storage in saline, Aquifers, Journal of Physics: Conference Series 78, 012042 doi:10.1088/1742-6596/78/1/012042.

748 Medina, C., Barnes, D., Rupp, J., 2008. Depth Relationships in Porosity and Permeability in the
749 Mount Simon Sandstone of the Midwest Region: Applications for Carbon Sequestration:
750 Eastern Section Meeting of the American Association of Petroleum Geologists, Pittsburgh, PA.
751 McIntosh, J.C., Walter, L.M., Martini, A. M., 2004. Extensive microbial modification of formation
752 water geochemistry: Case study from a Midcontinent sedimentary basin, United States.
753 Geological Society of America Bulletin. 116, 743-759.
754 Medina, C.R., Barnes, D.A., Rupp, J.A., 2008. Depth Relationships in Porosity and Permeability in
755 the Mount Simon Sandstone (Basal Sand) of the Midwest Region: Applications for Carbon
756 Sequestration (Poster, AAPG-SPE Eastern Meeting, 11 - 15 October 2008, Pittsburgh,
757 Pennsylvania).
758 Neuzil, C.E., 2000. Osmotic generation of 'anomalous' fluid pressures in geological environments.
759 Nature. 403, 182-184.
760 Nicholson C., Roeloffs, E., Wesson, R.L., 1988. The Northeastern Ohio Earthquake of 31 January
761 1986: was it induced? Bulletin of the Seismological Society of America 78, 188-217.
762 Nicholson, C., Wesson, R.L., 1990. Earthquake hazard associated with deep well injection: A report to
763 the U.S. Environmental Protection Agency. U.S. Geological Survey Bulletin 1951, 74 pp., U.S.
764 Geological Survey, Reston, Va.
765 Nordbotten, J., Celia, M., Bachu, S., Dahle, H., 2005. Semi-analytic solution for CO_2 leakage through
766 an abandoned well. Environmental Science and Technology. 39, 602-611.
767 Nordbotten, J., Celia, M., Bachu, S., 2004. Analytical solution for leakage rates through abandoned
768 wells. Water Resources Research. 40, WO4204.
769 Nordbotten, J.M., Kavetski, D., Celia, M.A., Bachu, S., 2008. A Semi-analytical Model Estimating
770 Leakage associated with CO_2 Storage in Large-scale Multilayered Geological Systems with
771 Multiple Leaky Wells, published online 17th December 2008, *Environmental Science and*
772 *Technology*, 2008.
773 Olcott, P.G., 1992. Ground Water Atlas of the United States, Segment 9--Iowa, Michigan, Minnesota,
774 and Wisconsin: U.S. Geological Survey Hydrologic Investigations Atlas 730-J, 31 p.

775 Obermeier, S.F., Munson, P.J., Munson, C.A., Martin, J.R., Frankel, A.D., Youd, T.L., Pond, E.C.,
776 1992. Liquefaction evidence for strong Holocene earthquake(s) in the Wabash Valley of
777 Indiana-Illinois. Seismological Research Letters. 63, 321-335.
778 Pawar, R., 2007. Multiphase Flow Simulations Of Large-Scale CO2 Sequestration Operation: How
779 Do You Incorporate Details Of Wellbores In Coarse Grids? American Institute of Chemical
780 Engineers, Annual Meeting, Salt Lake City, abstract 518b.
781 Person, M., Taylor, J., Dingman, S.L., 1998. Sharp-Interface Models of Salt Water Intrusion and Well
782 Head Delineation on Nantucket Island, Massachusetts. Ground Water. 36, 731-742.
783 Person, M, Roy, P., Wright, H., Ito, E, Winter, T, Rosenberry, D., Gutowski, W., Cohen, D., Morin,
784 P., 2007. Hydrologic Response of the Crow Wing Watershed, Minnesota to Mid-Holocene
785 Climate Change. Geological Society of America Bulletin. 119, 363-376.
786 Person, M.A., McIntosh, J., Bense, V.F., Remenda, V., Pleistocene Hydrology of North America: The
787 role of icesheets in reorganizing groundwater flow systems. Reviews of Geophysics. 45,
788 RG3007, doi:10.1029/2006RG000206, 2007.
789 Rhea, L., Person, M., de Marsily, G., Ledoux, E., Galli, A., 1994. Geostatistical Models of Secondary
790 Petroleum within Heterogeneous Carrier Beds: A Theoretical Example. American Association
791 of Petroleum Geologists. 78, 1679-1691.
792 Rubin, E., Meyer, L. and H. de Coninck, 2005. IPCC Special Report on Carbon Dioxide Capture and
793 Storage: Prepared by Working Group III of the Intergovernmental Panel on Climate Change,
794 Intergovernmental Panel on Climate Change, Cambridge.
795 Schlegel, M., McIntosh, J., Person, M., Ballentine, C., Zheng, Z., 2008. Investigating the source and
796 timing of freshwater recharge into saline aquifers in the glaciated Illinois Basin, Geochimica et
797 Cosmochimica Acta. 72, A832.
798 Seeber, L., Armbruster, J.G., Kim, W.Y., 2004. A fluid-injection-triggered earthquake sequence in
799 Ashtabula, Ohio: Implications for seismogenesis in stable continental regions. Bulletin of the
800 Seismological Society of America. 24, 76-87.

Stueber, A.M., Walter, L.M., 1994. Glacial Recharge and Paleohydrologic Flow Systems in the Illinois Basin - Evidence From Chemistry of Ordovician Carbonate (Galena) Formation Waters. Geological Society of America Bulletin. 106, 1430-1439.

Taylor, J., Person, M., 1996. Capture Zone delineation on island aquifer systems. Ground Water. 36, 722-730.

Walton, W.C., 1960. Leaky artesian aquifer conditions in Illinois, Illinois State Water Survey Report Investigation 39, 27 pp.

Walton, W. C., 1962. Future water-level declines in deep sandstone wells in Chicago Region. Ground Water. 2, 13-20.

Wheeler, R.L., Cramer, C.H, 2002. Updated seismic hazard in the southern Illinois Basin; geological and geophysical foundations for use in the 2002 USGS national seismic-hazard maps. Seismological Research Letters. 73, 776-791.

Witherspoon, P., Neuman, S., 1967. Evaluating a lightly permeable caprock in aquifer gas storage, 1: Caprock of infinite thickness. Trans. AIME. 240, 949.

Witherspoon, P.A., Mueller, T. D., Donovan, R.W., 1962. Evaluation of underground gas storage conditions in aquifers through investigations of groundwater hydrology. Journal of Petroleum Technology. 14, 555-562.

Zoback, M.D., Hickman, S., 1982. In-situ study of the physical mechanisms controlling induced seismicity at Monticello Reservoir, South Carolina. Journal of Geophysical Research. 87, 6959-6974.

Zoback, M.D., Zoback, M.L., 1989. In situ stress, crustal strain and seismic hazard assessment in eastern North America, Earthquake Hazards and the Design of Constructed Facilities in the Eastern United States (K.H. Jacob & C.J. Turkstra, eds.), Annals of the New York Academy of Sciences, v. 558, p. 54-65, N.Y. Acad. Sci., NY, 1989, 457 pp.

825 Zoback, M.D., Zoback, M.L., 1989. State of stress in the earth's lithosphere. In Encyclopedia of Solid
826 Earth Geophysics (D.E. James, ed.), Encyclopedia of Earth Sciences Series (R.W. Fairbridge,
827 Series Ed.), Van Nostrand Reinhold Co., New York, 1221-1232.

828 Zoback, M.D., Zoback, M.L., 1989. Tectonic stress field of the continental U.S. In Geophysical
829 Framework of the Continental United States (eds. L. Pakiser and W. Mooney), GSA Memoir,
830 172, 523-539.

831 Zoback, M.D., Harjes, H.-P., 1997. Injection induced earthquakes and crustal stress at 9 km depth at
832 the KTB deep drilling site, Germany. Journal of Geophysical Research. 102, 18,477-18,491.

833

7. Figure Captions

Figure 1. (A) Location and capacity of coal fired power plants across Illinois Basin. The outline of the model domain is indicated by the red trapizoid (source: http://www.midcarb.org).(B) Changes in porosity, permeability and thickness of the Mount Simon and Eau Claire confining units with depth along A-A' shown in (A).(C) Illustration of injection well spacing at power plants represented in our sharp interface model.

Figure 2. (A) Locations, estimated magnitudes, and age of Holocene earthquake activity across southern Illinois Basin. Major fault systems include the Rough Creek (RC) and Lusk Creek (LC) Fault Systems. The shaded patterns denote active fault systems or seismogenic zones. Earth quake magnitudes and ages are based on scale and ^{14}C age dates of liquefaction features such as sand dikes in the vicinity of fault systems (after Wheeler and Cramer, 2002). The red circles denote the estimated earthquake magnitudes in the southern Illinois Basin. Blue lines indicated direction of maximum horizontal stress inferred from bore hole stress tests and borehole elongation data (from Nicholson and Wesson, 1990). (B) Location of earthquakes and hazardous waste injection wells in the Ohio-Pennsylvanian boarder, Mount Simon Formation. Injection of 320 L/min at a depth of 1.8 km resulted in up to 11 MPa of deviatoric pressures and are thought to have induced M2.6-M4.3 earthquakes (from Nicholson and Wesson, 1990).

Figure 3. Drawdown patterns (in meters) in Cambro-Ordovician aquifer system near Chicago (A) and in Mount Simon formation near Minneapolis/St Paul (B). Drawdrown patterns around Chicago also include Ironton galesville and Mount Simon formations (after Walton, 1960). Drawdown exceeds 183 m near Chicago and 45 m near Minneapolis/St. Paul due to municipal water well withdrawls which are on the same order of magnitude as CO_2 produced from power plants (squares in D). (C) Cumulative freshwater withdraws, Minneapolis/St Paul. (D) Basemap showing location of powerplants. Boxes show location of Figures 3A and 3B. (after Olcott, 1992; Lloyd and Lyke, 1995).

Figure 4. Plan-view (A) and cross-sectional (B) representation of Illinois basin stratigraphy. This study focuses on hydrodynamics within the basal Mount Simon aquifer and overlying Eau Claire confining unit.

Figure 5. Spatial variations in elevation of the top of the Mount Simon Formation across the Illinois Basin.

Figure 6. Spatial variations in the thickness (in meters) of Mount Simon Formation the Illinois Basin.

Figure 7. N-S cross section in western Indiana showing gamma ray curves (in red) and porosity curves (in blue). A preliminary subdivision of the Mount Simon Sandstone (orange, yellow) and overlying Eau Clair confining unit (gray) is shown based primarily on gamma logs. Our analysis focuses on the orange middle unit which exhibits highest permeability values.

Figure 8. (A) Mount Simon head and (B) salinity patterns across Illinois Basin and (C) salinity-depth profiles within Illinois Basin (Figure 8A after Gupta and Bair, 1999).

Figure 9. TOUGH2 simulation of pore pressures for Mount Simon formation resulting from injection of 390 MT/year of supercritical CO_2 using 26 wells located in the center of the Illinois Basin after a period of 30 years (after Birkholzer et al. 2007). Injection pressures reached 30 Bars (3 MPa) and propagated to basin margins (~200 km). The CO_2 was injected into a sub-member of the Mount Simon with an assigned permeability of 1000 mD. The location of the sharp interface model (Sharp_CO2) domain presented in this study is also shown.

Figure 10. Porosity-depth relationship for the Mount Simon sandstone based on core analyses of 128 wells and geophysical logs from 189 additional wells. These data indicate an (Athy type) exponential relationship exists between porosity and depth (Medina et al, 2008).

887

888 **Figure 11.** Porosity-Permeability data for Mount Simon Formation shows a log-linear positive
889 relationship between porosity and permeability (Medina et al, 2008).

890

891 **Figure 12.** Schematic diagram depicting variables and processes represented by sharp interface model
892 of Illinois Basin.

893 **Figure 13.** Comparison of PFLOTRAN/FEHM (A,B) and Sharp-CO_2 (C,D) models. A single well
894 injecting 2.3 kg/s of supercritical CO_2 into a confined aquifer for a period of 10 years is represented in
895 this test case. Vertically averaged heads and interface positions were estimated from (A,B) and
896 compared to sharp-interface model (C,D).

897

898 **Figure 14.** Analytical calculations of CO_2 injection into the Mount Simon reservoir with leakage
899 across the overlying Eau Clair confining unit using leaky aquitard solution of Hantush and Jacob
900 (1955). Fluid was injected at a constant rate of $2.2 \cdot 10^5$ m^3/day (A,B,C) and $2.75 \cdot 10^4$ m^3/day (D)
901 continuously for a period of 100 years (A,B,C) and 30 years (D). The numbers on the lines (Figures
902 14A,B,C,D) are years since the onset of injection. Note that the horizontal axis limits of Figures 14A-
903 C differs from Figure 14D.

904

905 **Figure 15.** Basin-scale (A), and intermediate-scale (B-C) finite element grids of CO2-brine transport,
906 Illinois Basin.

907

908 **Figure 16.** Basin scale simulated deviatoric fluid pressures (in MPa) after 100 years of injection (A)
909 and 100 years of shutin (B).

910

911 **Figure 17.** Deviatoric pressures at deep (A) and intermediate (C) depths within the Illinois Basin after
912 injection of 100 million metric tons of CO_2 using 726 injection wells over a 100 year period using

913 refined grids. Fluid pressures after 100 years of shutin (200 years) are presented in Figure 16B and
914 16D for deep and intermediate depths. The locations of the models are shown in Figure 16.
915
916 **Figure 18.** Simulated CO_2 lens thickness at (deep and intermediate) depths across the Illinois basin
917 after 100 years of continuous injection of 80 million metric tons of CO_2 using 726 injection wells. The
918 locations of these models are shown in Figure 16.
919
920 **Figure 19.** Simulated lateral brine displacement rates (A,B) and vertical (C,D) brine leakage through
921 the Eau Claire Formation (in m/day) after 100 years of continuous injection of 80 million metric tons
922 of CO_2 using 726 injection wells.
923
924 **Figure 20**. Computed fluid pressure verses depth for intermediate (1700-200 m depth) and deep
925 (2900-3500 m depth) reservoirs. Deviatoric pressure reached about 46% of lithostatic levels in the
926 deepest part of the basin after 100 years of continuous CO_2 injection. Also plotted (circle) is inferred
927 pressure and depth within Mount Simon near Ashtabula, Ohio which is believed to have produced
928 M2.6-M4.3 earthquakes between 1987-2001 as a result of 10MPa of deviatoric pressures associated
929 with hazardous waste injection (Ashtabula, OH pore pressures are from Nicholson and Wesson,
930 1990).
931
932 **Figure 21.** Computed uplift at the land surface after 100 years of continuous CO_2 injection.
933
934 **Figure 22.** Plan view contour map of Hubbert CO_2 heads (in m) and separate phase CO_2 migration
935 directions (lines with arrows) due to buoyancy and hydrodynamic effects. Stream traces indicate that
936 most of the CO_2 would be captured in gentle structural traps at the intermediate depth within the
937 Illinois Basin.
938
939

8. Tables

Table 1. Aquifer and Confining Unit properties used in Sensitivity Analysis

Run	UNIT	*k/k'	k (mD)	k' (mD)	+b (m)	#b' (m)	$S
1	Mount Simon	50000	50	0.0010	500	50	0.05
1	Eau Claire		50	0.0010			
2	Mount Simon	1250000	125	0.0001	500	50	0.05
2	Eau Claire		125	0.0001			
3	Mount Simon	50	5	0.1000	500	50	0.05
3	Eau Claire		5	0.1000			

*k/k' ratio of horizontal to vertical permeability for the Mount Simon and Eau Clair
+ saturated thickness of the Mount Simon, # b' saturated thickness of the Eau Claire
$Storativity of Mount Simon assuming CO_2 dominated fluid phase

Table 2. Fluid, Rock, and Injection Well Properties used in Illinois Basin Simulations

CO_2 Viscosity	0.004 mPa-s
CO_2 Density	500 kg/m^3
Brine Viscosity	0.25 mPa-s
Brine Density	1,100 kg/m^3
Injection well Radius	0.15 m
Injection Well Rate	283.47 m^3/day
S_r	0.00

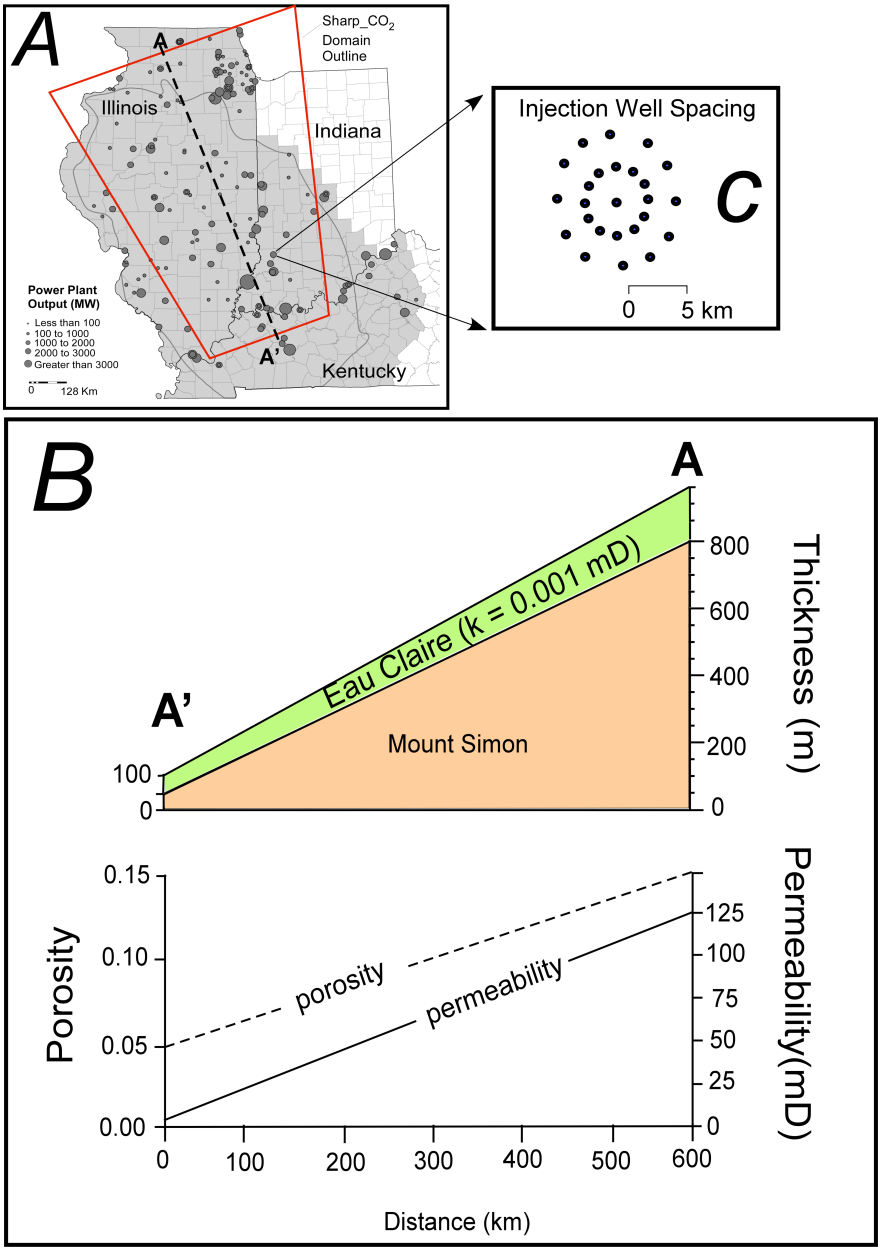
A
A
A'
Illinois
Indiana
Kentucky
Sharp_CO2
Domain
Outline
Power Plant
Output (MW)
Less than 100
100 to 1000
1000 to 2000
2000 to 3000
Greater than 3000
0
128 Km
Injection Well Spacing
C
0
5 km
B
A
A'
Eau Claire (k = 0.001 mD)
Mount Simon
100
0
800
600
400
200
0
Thickness (m)
Porosity
0.15
0.10
0.05
0.00
porosity
permeability
125
100
75
50
25
0
Permeability(mD)
0
100
200
300
400
500
600
Distance (km)

Figure 1

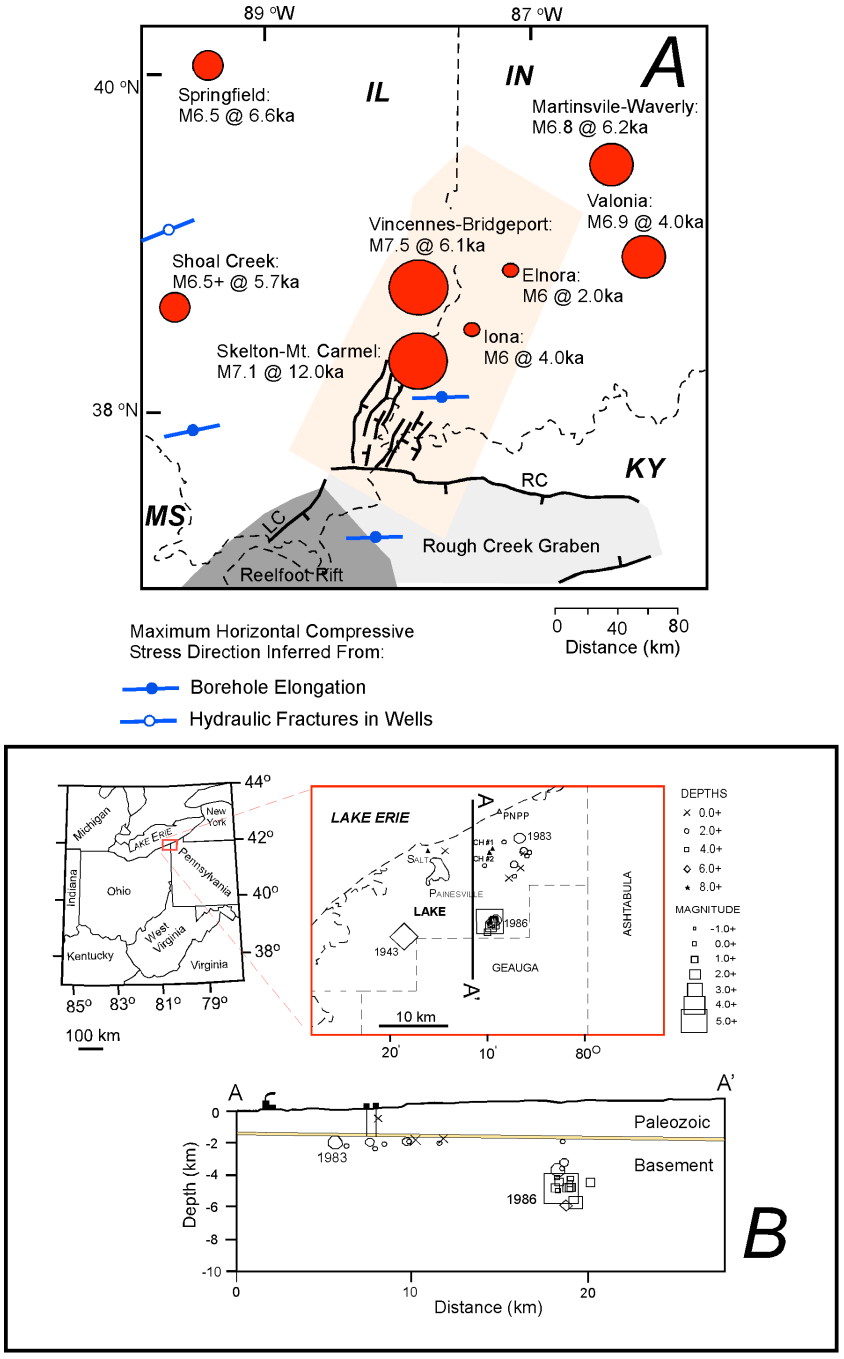
89 °W
87 °W
40 °N
38 °N
A
IL
IN
Springfield:
M6.5 @ 6.6ka
Martinsvile-Waverly:
M6.8 @ 6.2ka
Valonia:
M6.9 @ 4.0ka
Vincennes-Bridgeport:
M7.5 @ 6.1ka
Shoal Creek:
M6.5+ @ 5.7ka
Elnora:
M6 @ 2.0ka
Iona:
M6 @ 4.0ka
Skelton-Mt. Carmel:
M7.1 @ 12.0ka
KY
RC
MS
LC
Rough Creek Graben
Reelfoot Rift
0 40 80
Distance (km)
Maximum Horizontal Compressive
Stress Direction Inferred From:
Borehole Elongation
Hydraulic Fractures in Wells
44°
42°
40°
38°
85° 83° 81° 79°
100 km
Michigan
New York
Lake Erie
Pennsylvania
Indiana
Ohio
West Virginia
Kentucky
Virginia
LAKE ERIE
PNPP
1983
1986
1943
SALT
PAINESVILLE
LAKE
GEAUGA
ASHTABULA
10 km
20'
10'
80°
DEPTHS
0.0+
2.0+
4.0+
6.0+
8.0+
MAGNITUDE
-1.0+
0.0+
1.0+
2.0+
3.0+
4.0+
5.0+
A
A'
Paleozoic
Basement
Depth (km)
0
-2
-4
-6
-8
-10
0
10
20
Distance (km)
B

Figure 2

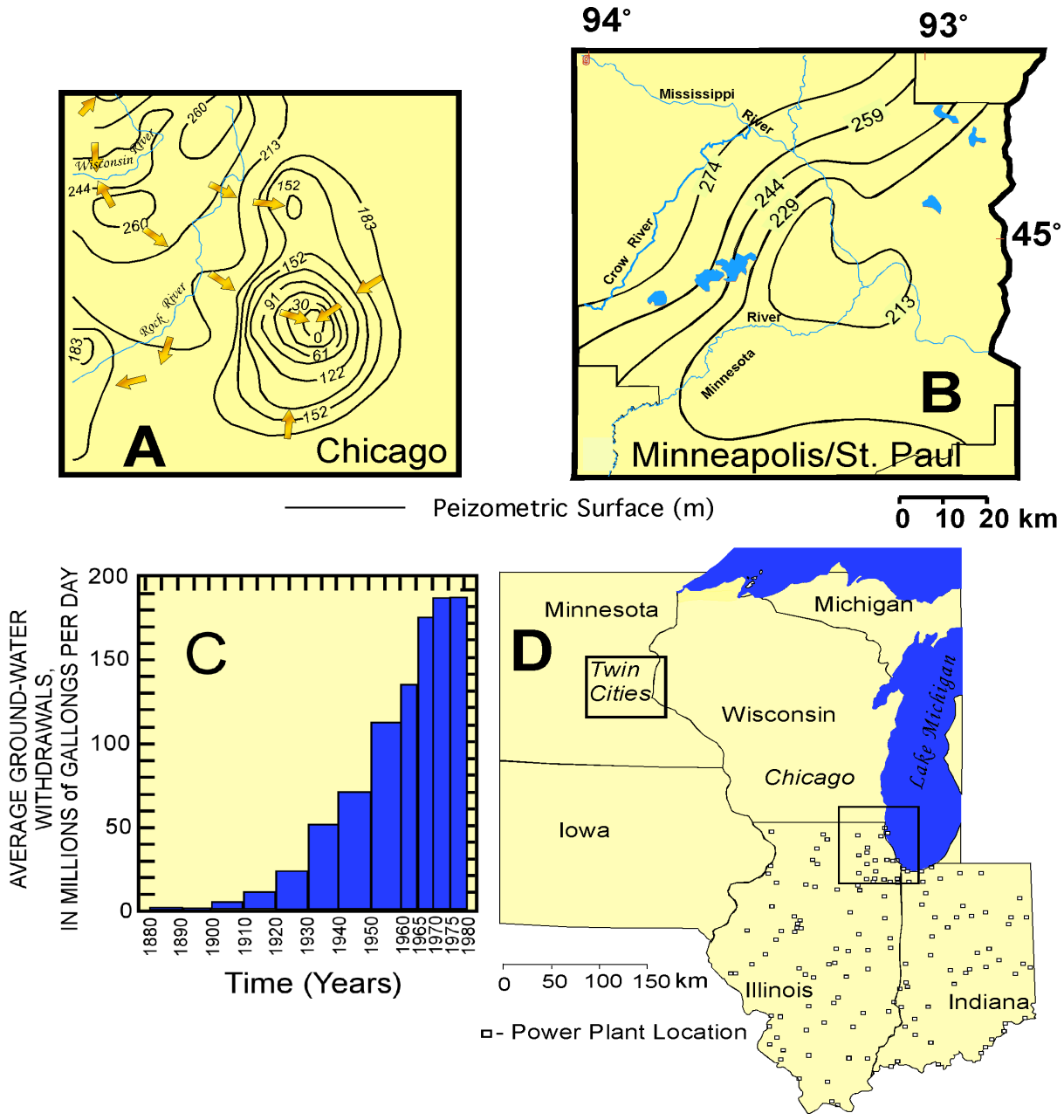
94°
93°
45°
Mississippi River
Wisconsin River
Rock River
Crow River
Minnesota River
A
Chicago
B
Minneapolis/St. Paul
Peizometric Surface (m)
0 10 20 km
C
AVERAGE GROUND-WATER WITHDRAWALS, IN MILLIONS of GALLONGS PER DAY
Time (Years)
D
Minnesota
Michigan
Twin Cities
Wisconsin
Chicago
Lake Michigan
Iowa
Illinois
Indiana
0 50 100 150 km
- Power Plant Location

Figure 3

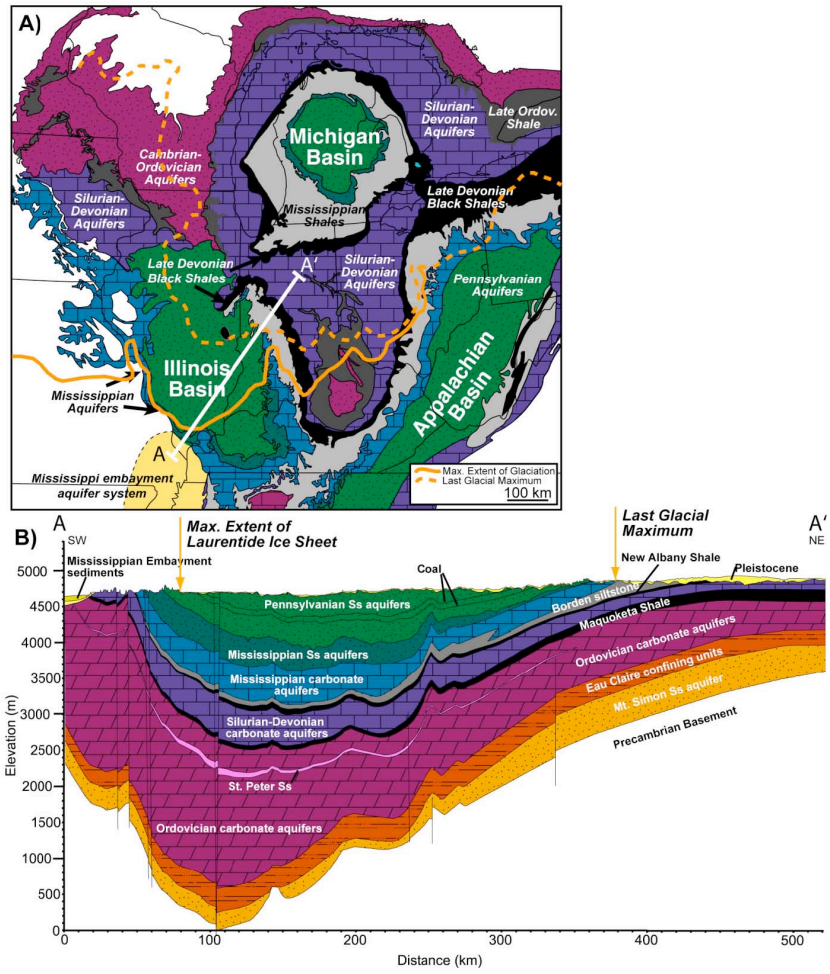
A)
Michigan Basin
Illinois Basin
Appalachian Basin
Cambrian-Ordovician Aquifers
Silurian-Devonian Aquifers
Late Ordov. Shale
Mississippian Shales
Late Devonian Black Shales
Pennsylvanian Aquifers
Mississippian Aquifers
Mississippi embayment aquifer system
A
A′
Max. Extent of Glaciation
Last Glacial Maximum
100 km
B)
SW
NE
Max. Extent of Laurentide Ice Sheet
Last Glacial Maximum
Mississippian Embayment sediments
Coal
New Albany Shale
Pleistocene
Borden siltstone
Maquoketa Shale
Ordovician carbonate aquifers
Eau Claire confining units
Mt. Simon Ss aquifer
Precambrian Basement
Pennsylvanian Ss aquifers
Mississippian Ss aquifers
Mississippian carbonate aquifers
Silurian-Devonian carbonate aquifers
St. Peter Ss
Ordovician carbonate aquifers
Elevation (m)
Distance (km)

Figure 4

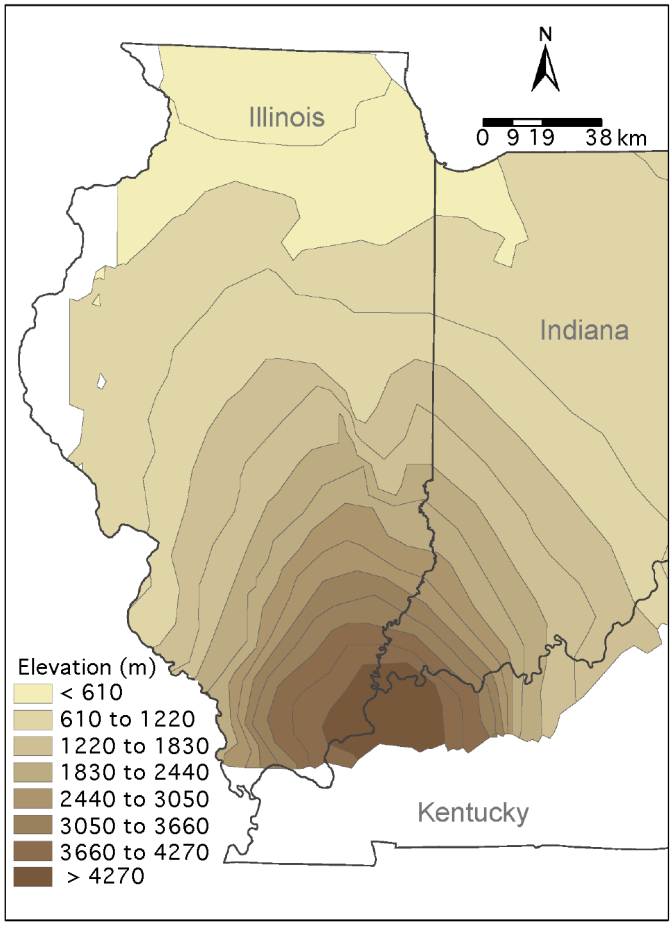
N
Illinois
0 9 19 38 km
Indiana
Kentucky
Elevation (m)
< 610
610 to 1220
1220 to 1830
1830 to 2440
2440 to 3050
3050 to 3660
3660 to 4270
> 4270

Figure 5

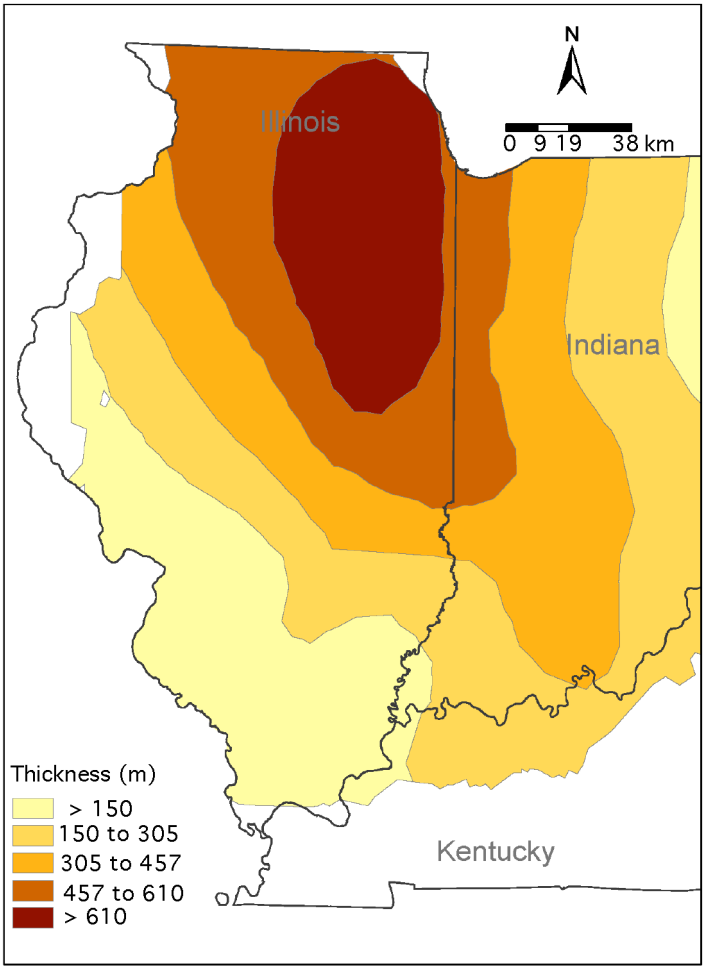
N
0 9 19 38 km
Illinois
Indiana
Kentucky
Thickness (m)
> 150
150 to 305
305 to 457
457 to 610
> 610

Figure 6

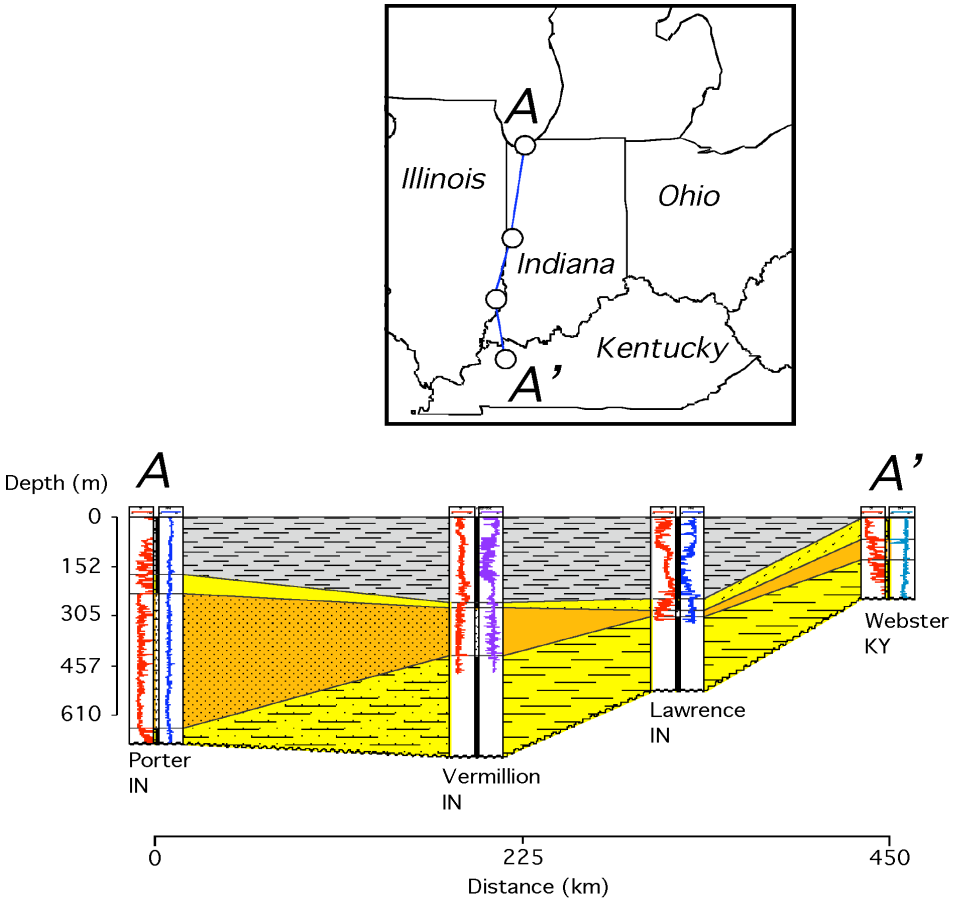
A
Illinois
Ohio
Indiana
Kentucky
A'
A
A'
Depth (m)
0
152
305
457
610
Porter
IN
Vermillion
IN
Lawrence
IN
Webster
KY
0
225
450
Distance (km)

Figure 7

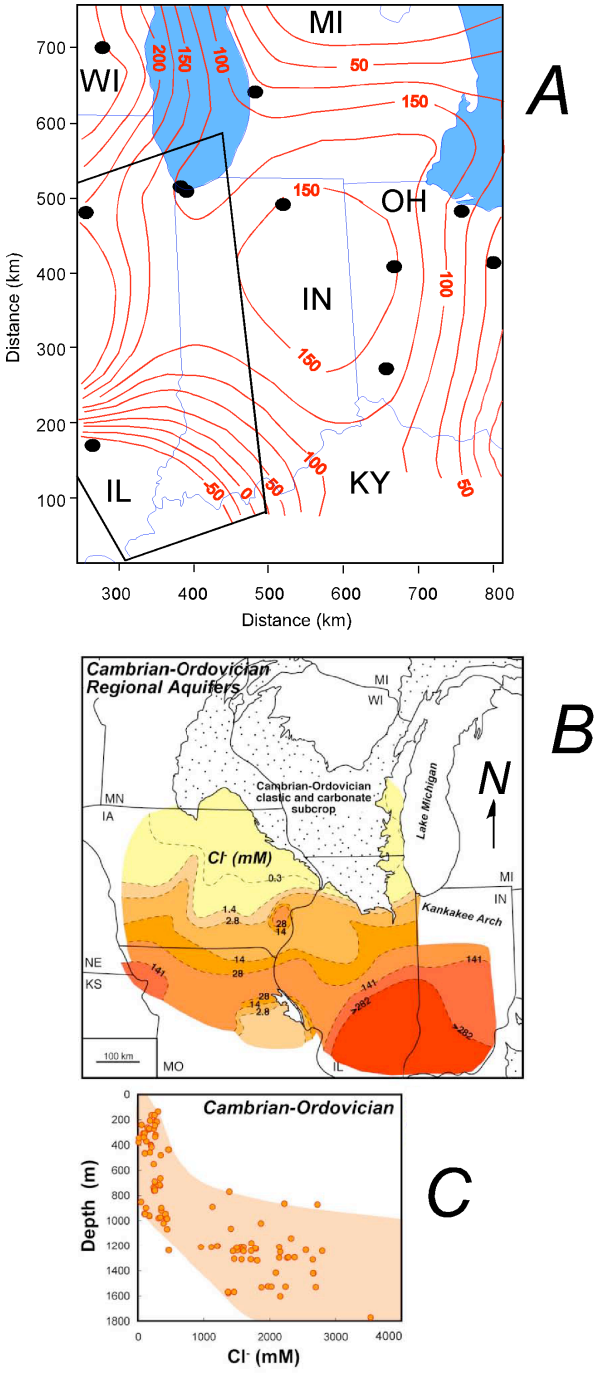
A
MI
WI
OH
IN
IL
KY
200
150
100
50
0
-50
Distance (km)
Distance (km)
B
Cambrian-Ordovician
Regional Aquifers
Cambrian-Ordovician
clastic and carbonate
subcrop
Lake Michigan
Kankakee Arch
Cl⁻ (mM)
MN
IA
NE
KS
MO
IL
IN
N
100 km
C
Cambrian-Ordovician
Depth (m)
Cl⁻ (mM)

Figure 8

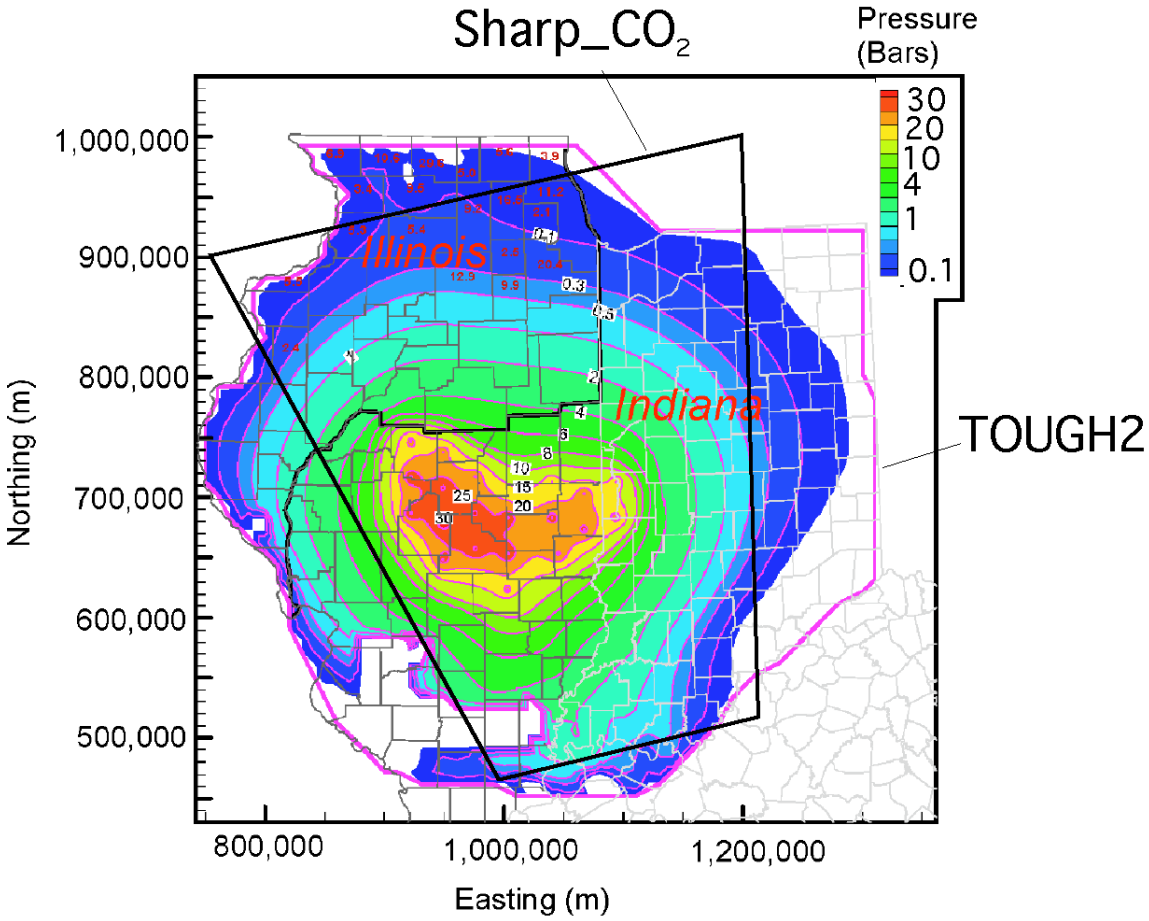
Sharp_CO2
Pressure
(Bars)
30
20
10
4
1
0.1
Illinois
Indiana
TOUGH2
1,000,000
900,000
800,000
700,000
600,000
500,000
Northing (m)
800,000
1,000,000
1,200,000
Easting (m)

Figure 9.

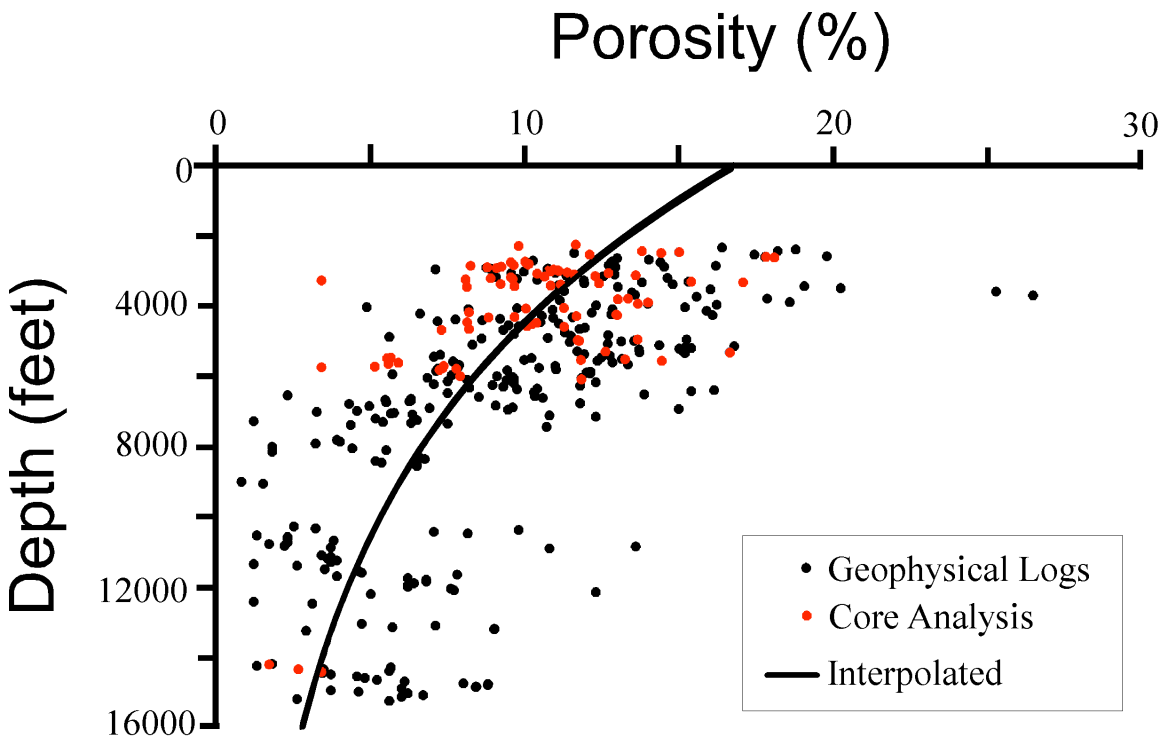
Porosity (%)
0
10
20
30
0
4000
8000
12000
16000
Depth (feet)
Geophysical Logs
Core Analysis
Interpolated

Figure 10

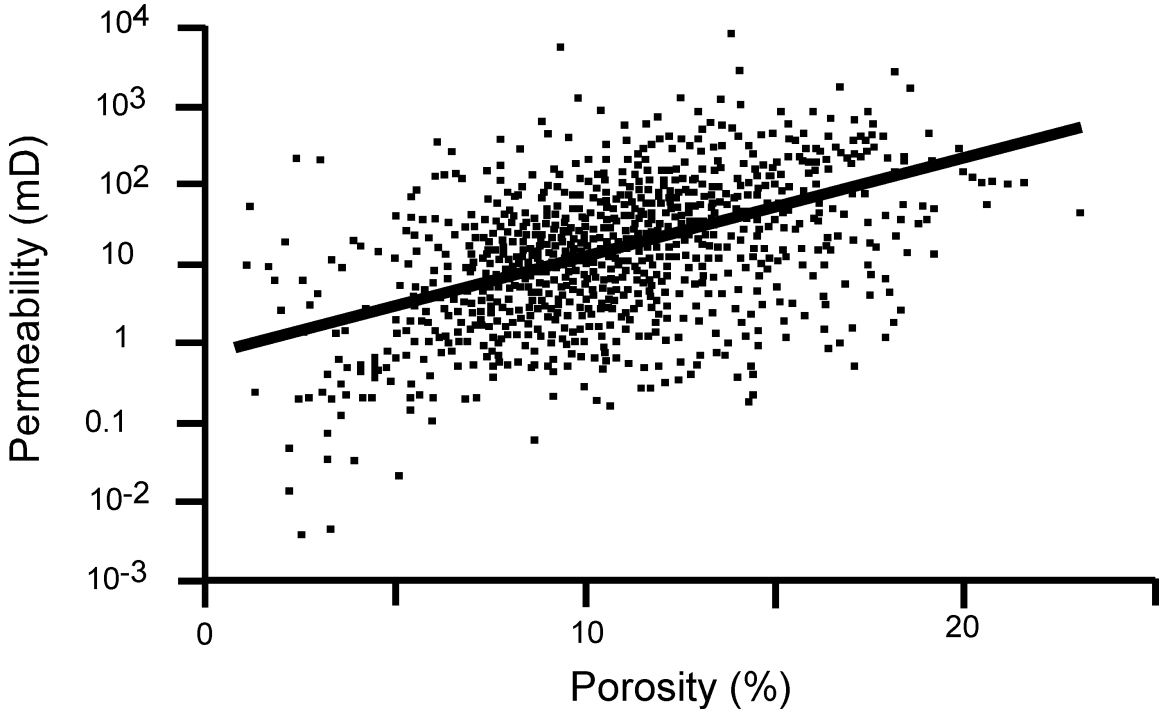

Figure 11

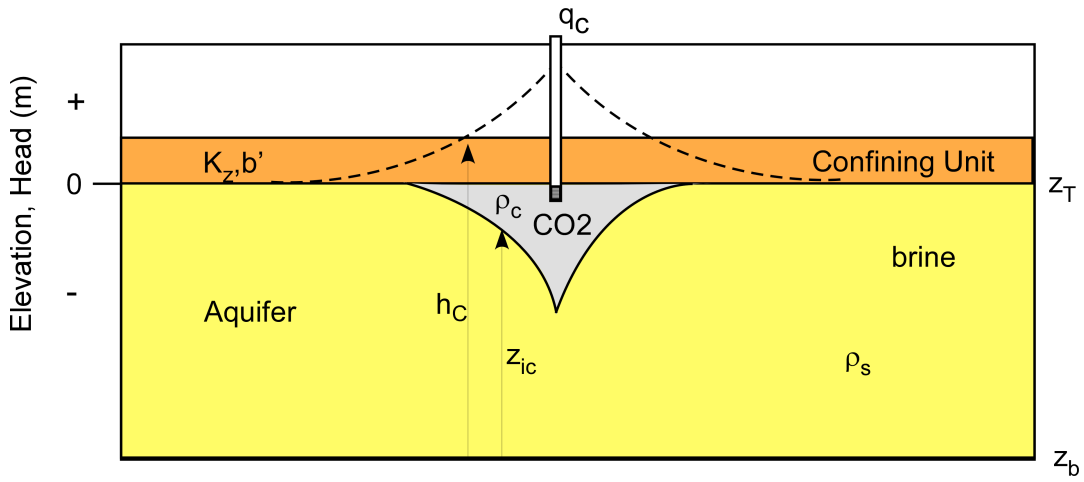
q_C
Elevation, Head (m)
+
0
-
K_z,b'
Confining Unit
z_T
ρ_c
CO2
brine
Aquifer
h_C
z_{ic}
ρ_s
z_b

Figure 12

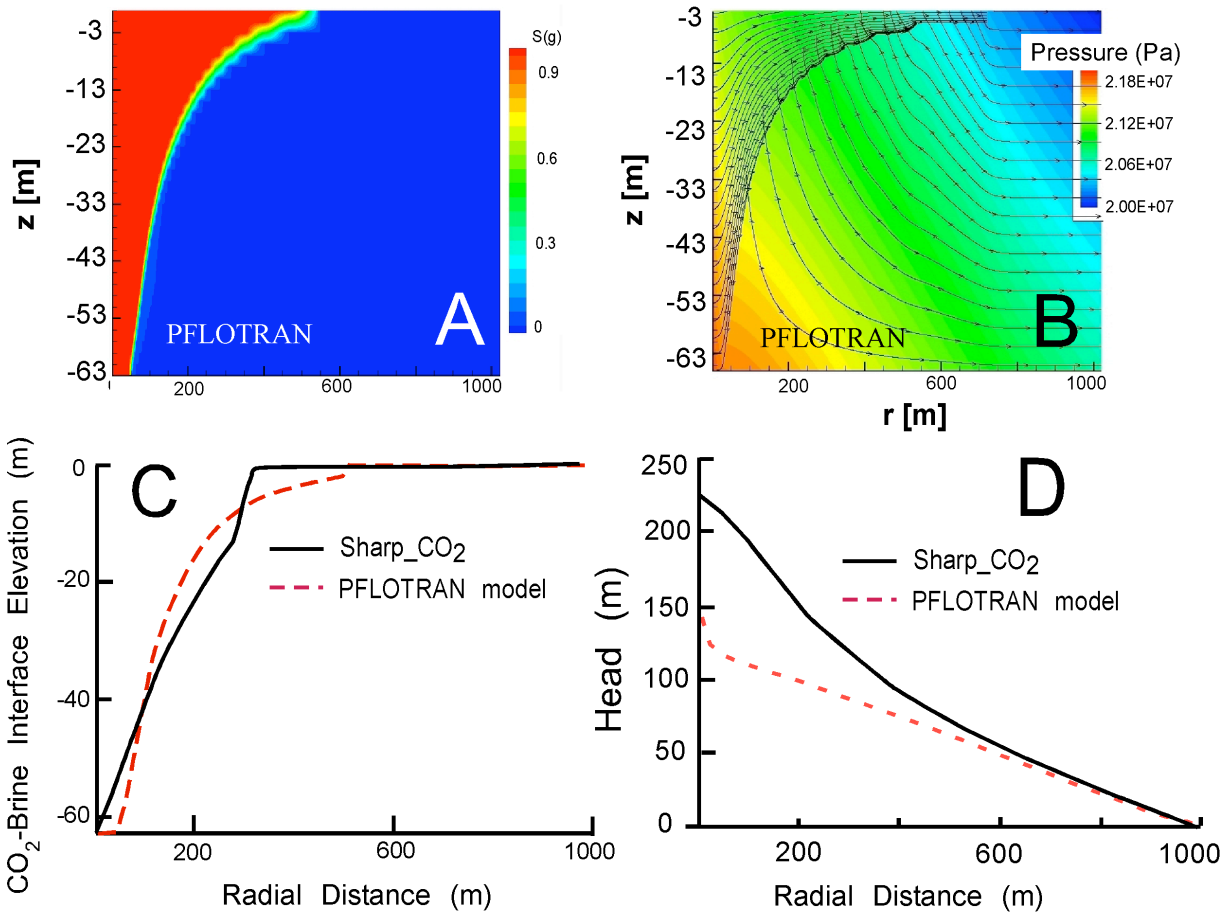
-3
-13
-23
-33
-43
-53
-63
z [m]
PFLOTRAN
A
S(g)
0.9
0.6
0.3
0
200
600
1000
Pressure (Pa)
2.18E+07
2.12E+07
2.06E+07
2.00E+07
B
r [m]
C
Sharp_CO2
PFLOTRAN model
CO2-Brine Interface Elevation (m)
Radial Distance (m)
D
Head (m)
250
200
150
100
50
0

Figure 13

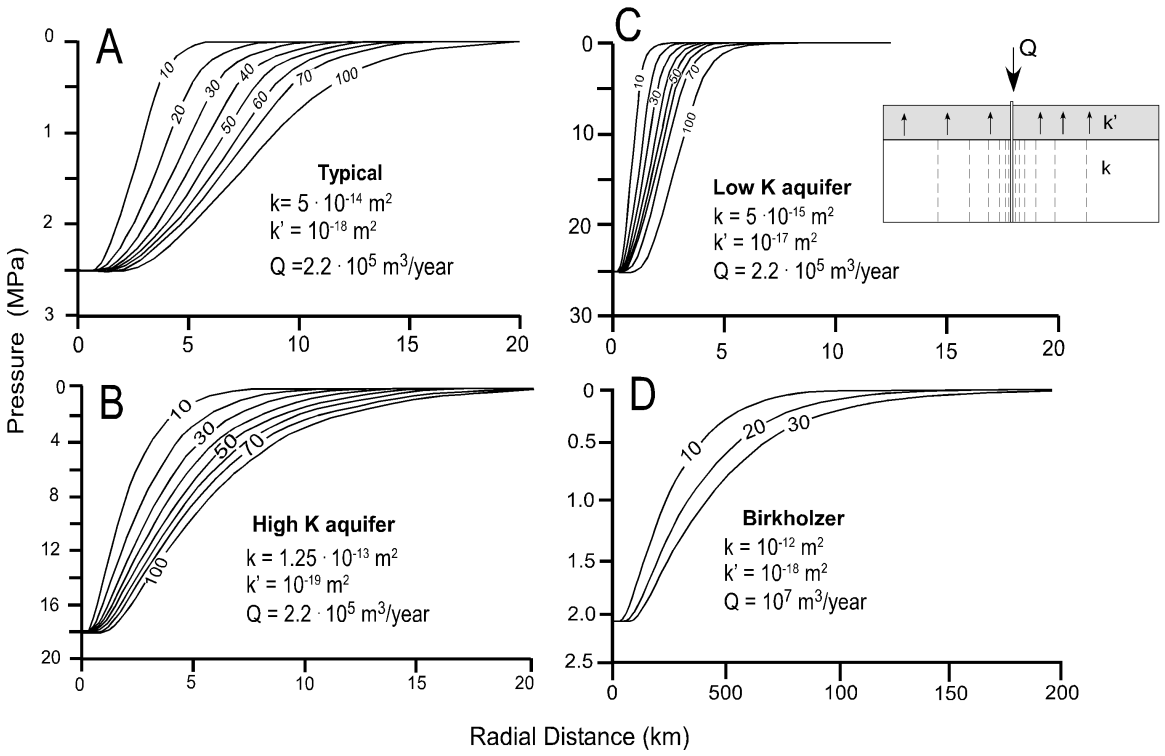
A
B
C
D
Pressure (MPa)
Radial Distance (km)
Typical
k= 5 · 10-14 m2
k' = 10-18 m2
Q =2.2 · 105 m3/year
High K aquifer
k = 1.25 · 10-13 m2
k' = 10-19 m2
Q = 2.2 · 105 m3/year
Low K aquifer
k = 5 ·10-15 m2
k' = 10-17 m2
Q = 2.2 · 105 m3/year
Birkholzer
k = 10-12 m2
k' = 10-18 m2
Q = 107 m3/year
Q
k'
k

Figure 14

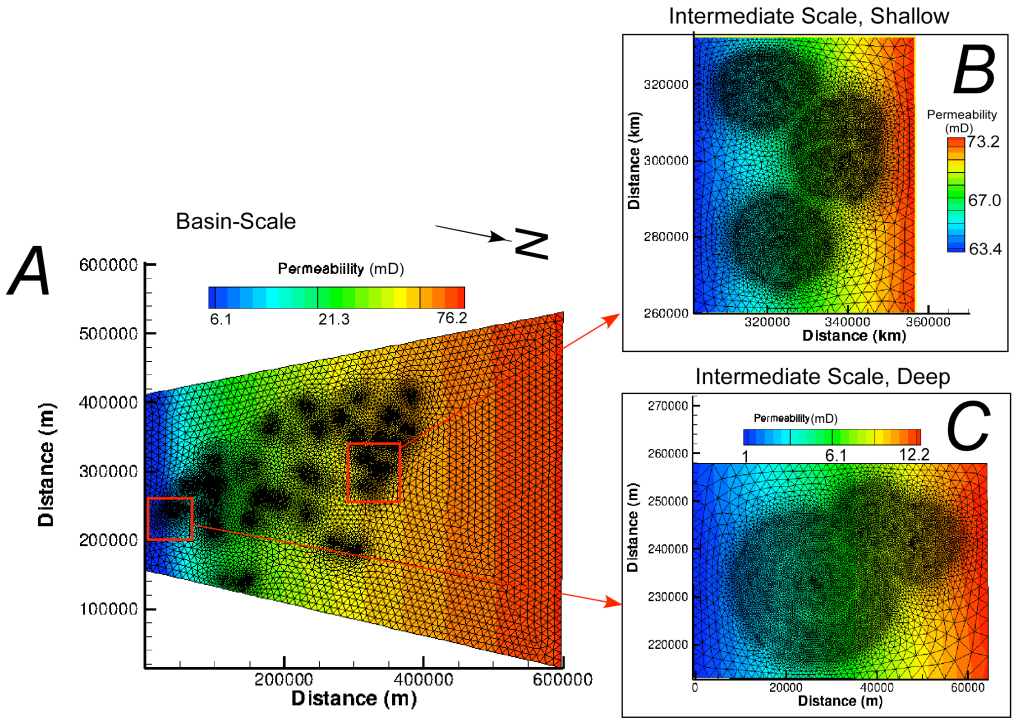
Intermediate Scale, Shallow
B
Permeability (mD)
73.2
67.0
63.4
Distance (km)
320000
300000
280000
260000
340000
360000
Basin-Scale
A
N
Permeability (mD)
6.1
21.3
76.2
Distance (m)
600000
500000
400000
300000
200000
100000
Intermediate Scale, Deep
C
Permeability (mD)
1
6.1
12.2
270000
260000
250000
240000
230000
220000
0
20000
40000
60000

Figure 15

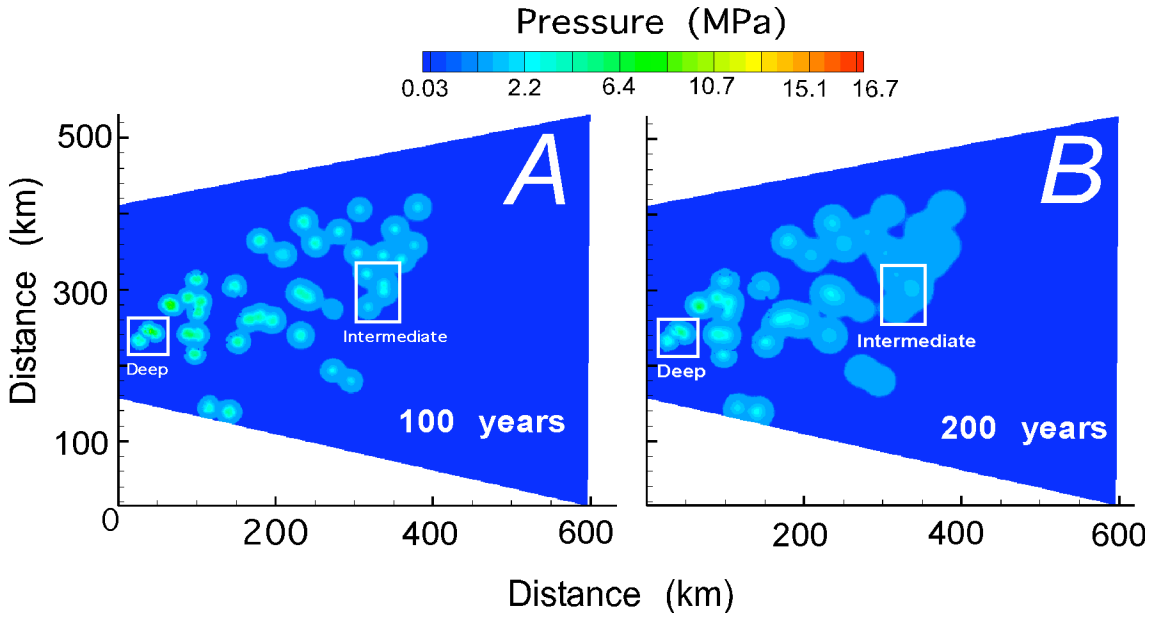
Pressure (MPa)
0.03
2.2
6.4
10.7
15.1
16.7
A
B
Intermediate
Deep
100 years
200 years
Distance (km)
500
300
100
0
200
400
600
Distance (km)

Figure 16

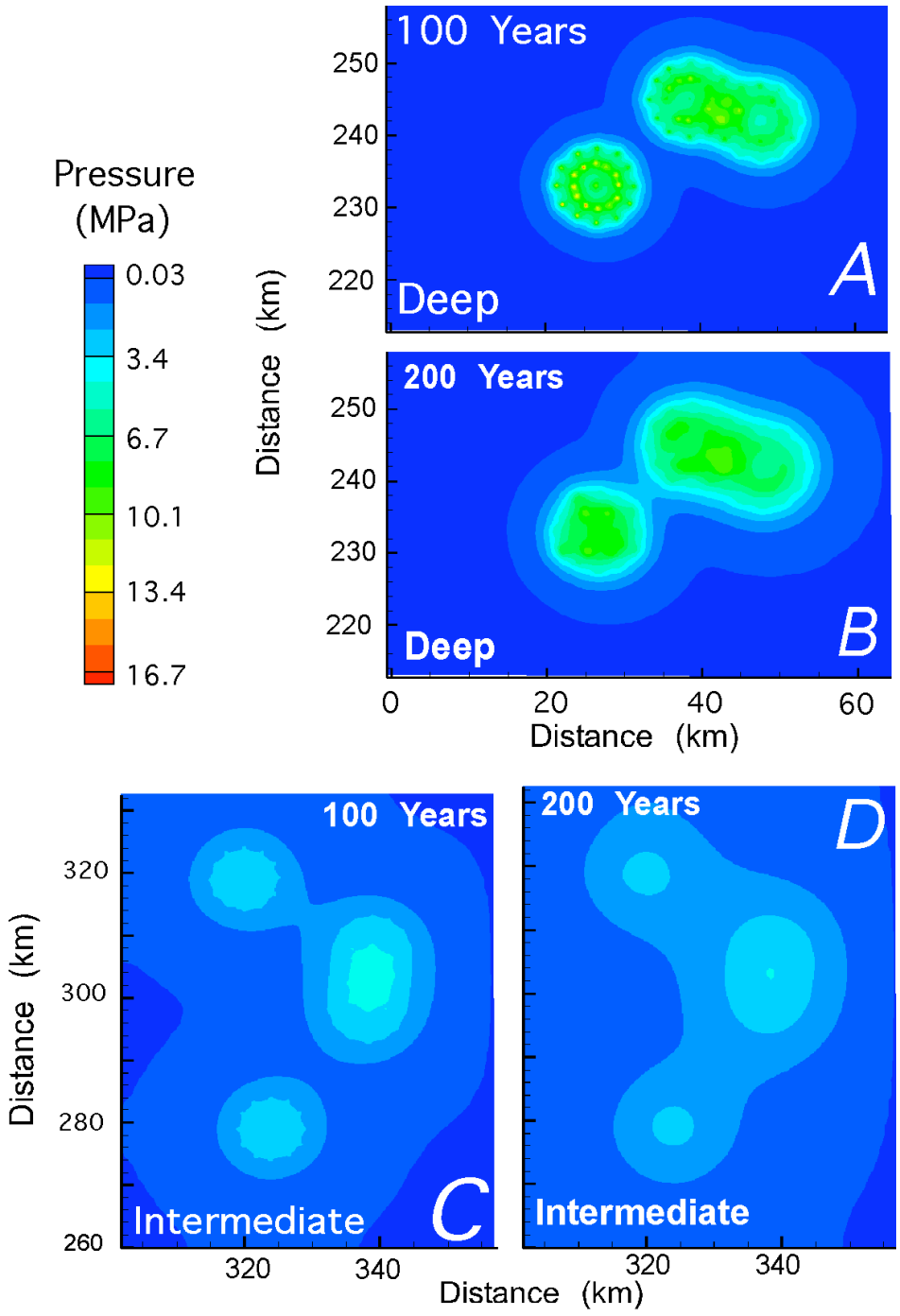
Pressure
(MPa)
0.03
3.4
6.7
10.1
13.4
16.7
100 Years
Deep
A
200 Years
Deep
B
Distance (km)
250
240
230
220
0
20
40
60
Distance (km)
100 Years
Intermediate
C
200 Years
Intermediate
D
Distance (km)
320
300
280
260
320
340
320
340
Distance (km)

Figure 17

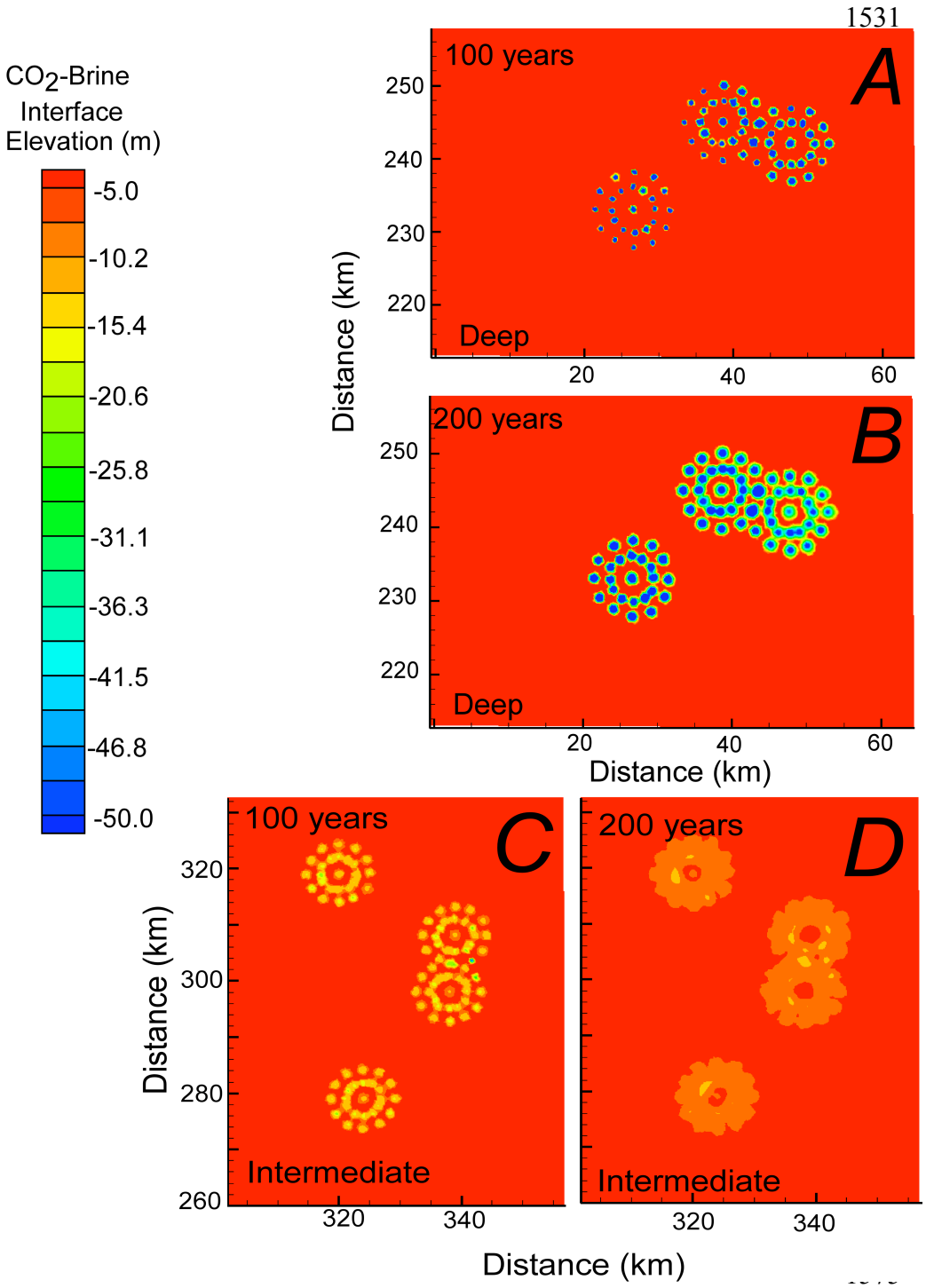
CO2-Brine
Interface
Elevation (m)
-5.0
-10.2
-15.4
-20.6
-25.8
-31.1
-36.3
-41.5
-46.8
-50.0
100 years
A
Deep
200 years
B
Deep
Distance (km)
100 years
C
Intermediate
200 years
D
Intermediate
Distance (km)
Distance (km)

Figure 18

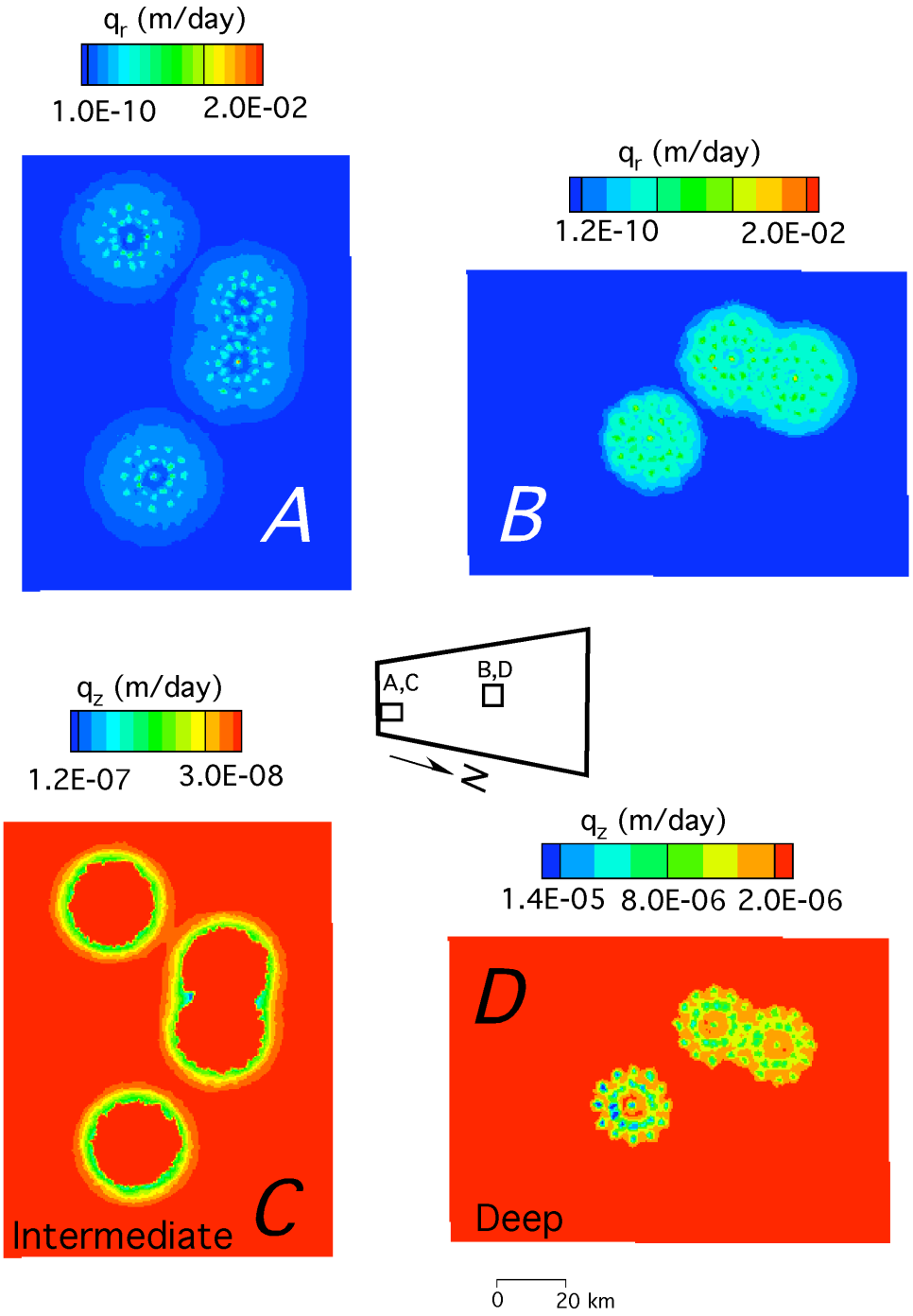
q_r (m/day)
1.0E-10
2.0E-02
A
q_r (m/day)
1.2E-10
2.0E-02
B
A,C
B,D
N
q_z (m/day)
1.2E-07
3.0E-08
Intermediate
C
q_z (m/day)
1.4E-05 8.0E-06 2.0E-06
D
Deep
0
20 km

Figure 19

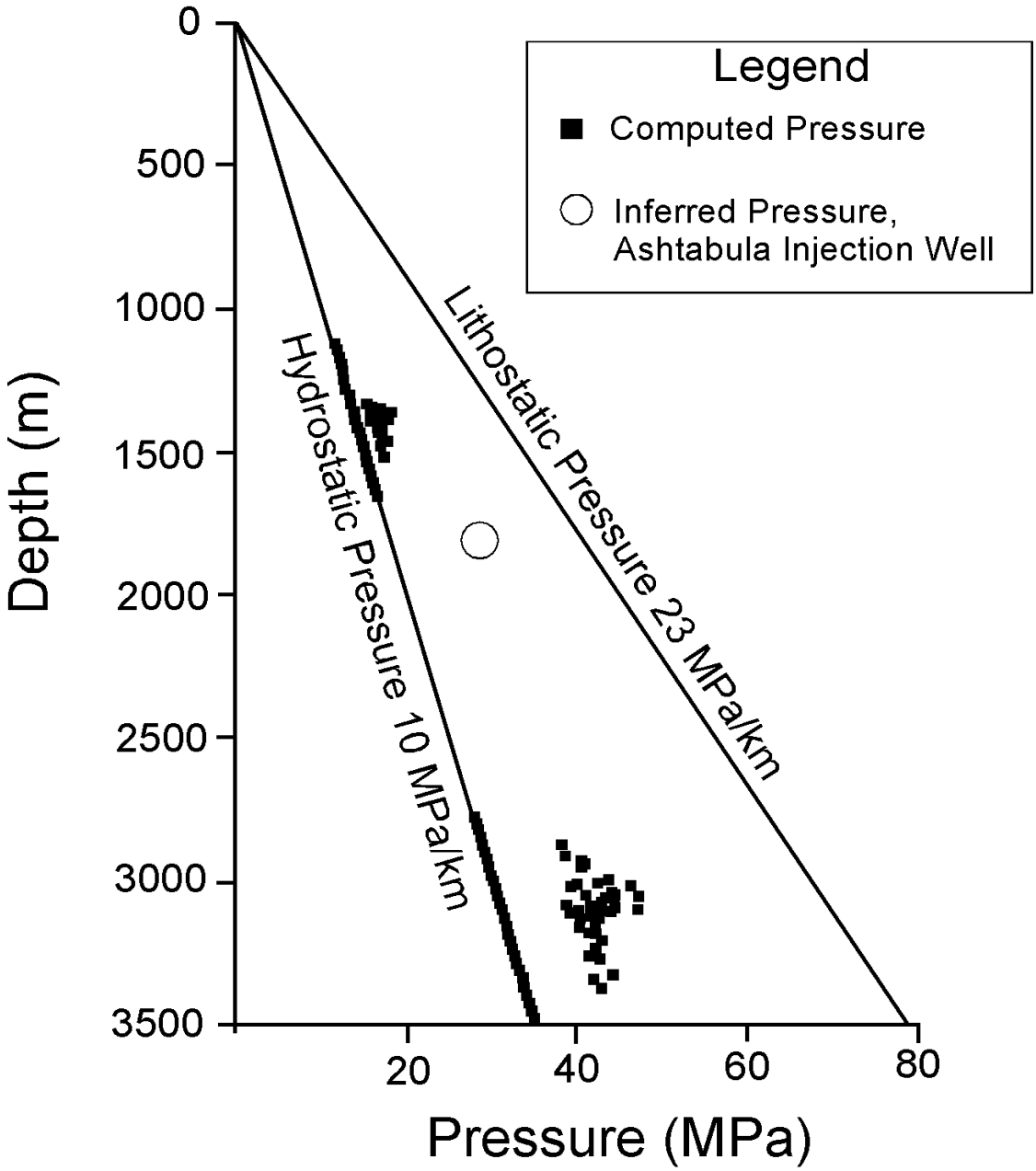
Legend
Computed Pressure
Inferred Pressure,
Ashtabula Injection Well
Lithostatic Pressure 23 MPa/km
Hydrostatic Pressure 10 MPa/km
Depth (m)
0
500
1000
1500
2000
2500
3000
3500
20
40
60
80
Pressure (MPa)

Figure 20

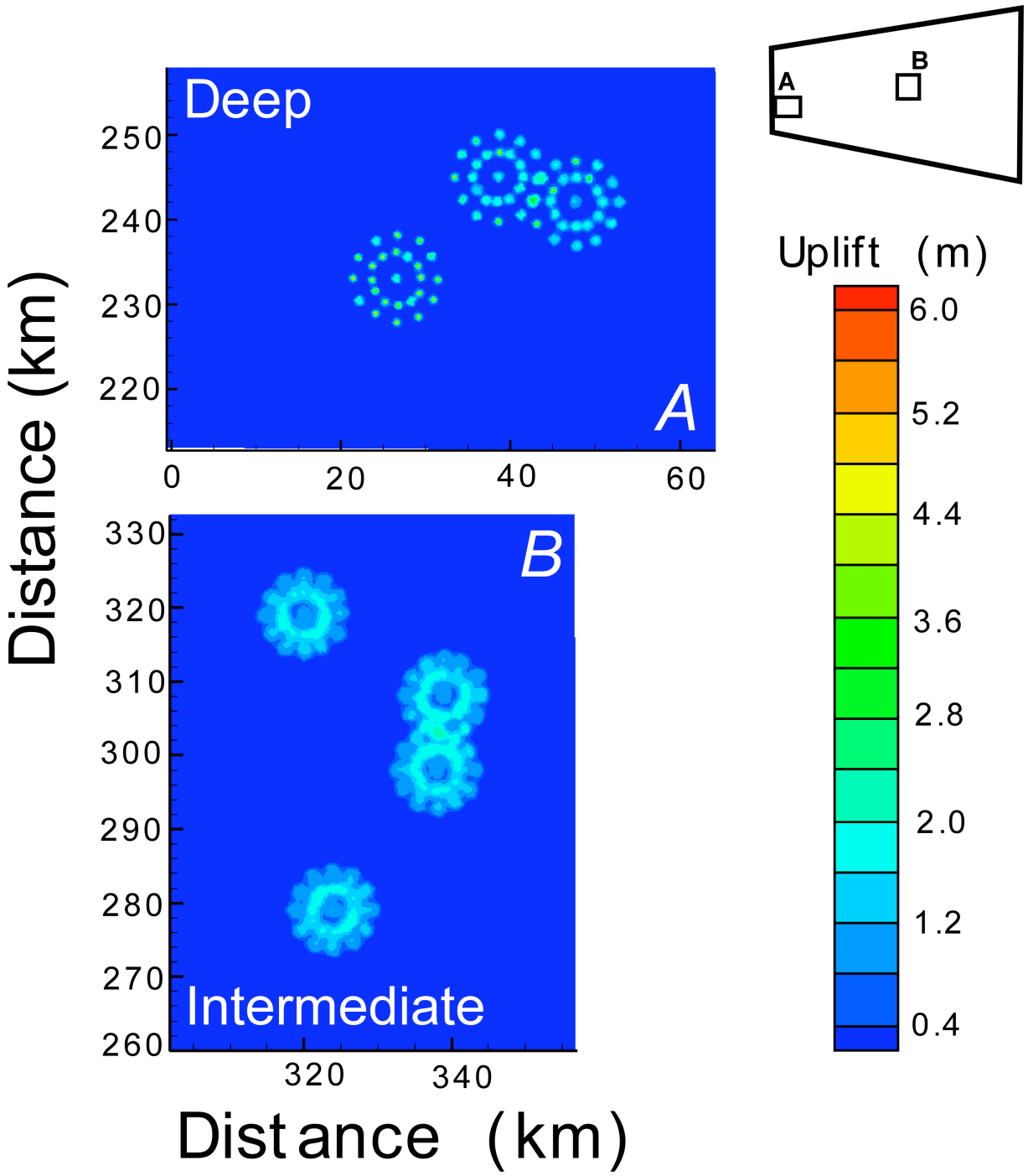
Deep
A
B
Intermediate
Distance (km)
Distance (km)
250
240
230
220
0
20
40
60
330
320
310
300
290
280
270
260
320
340
Uplift (m)
6.0
5.2
4.4
3.6
2.8
2.0
1.2
0.4
A
B

Figure 21

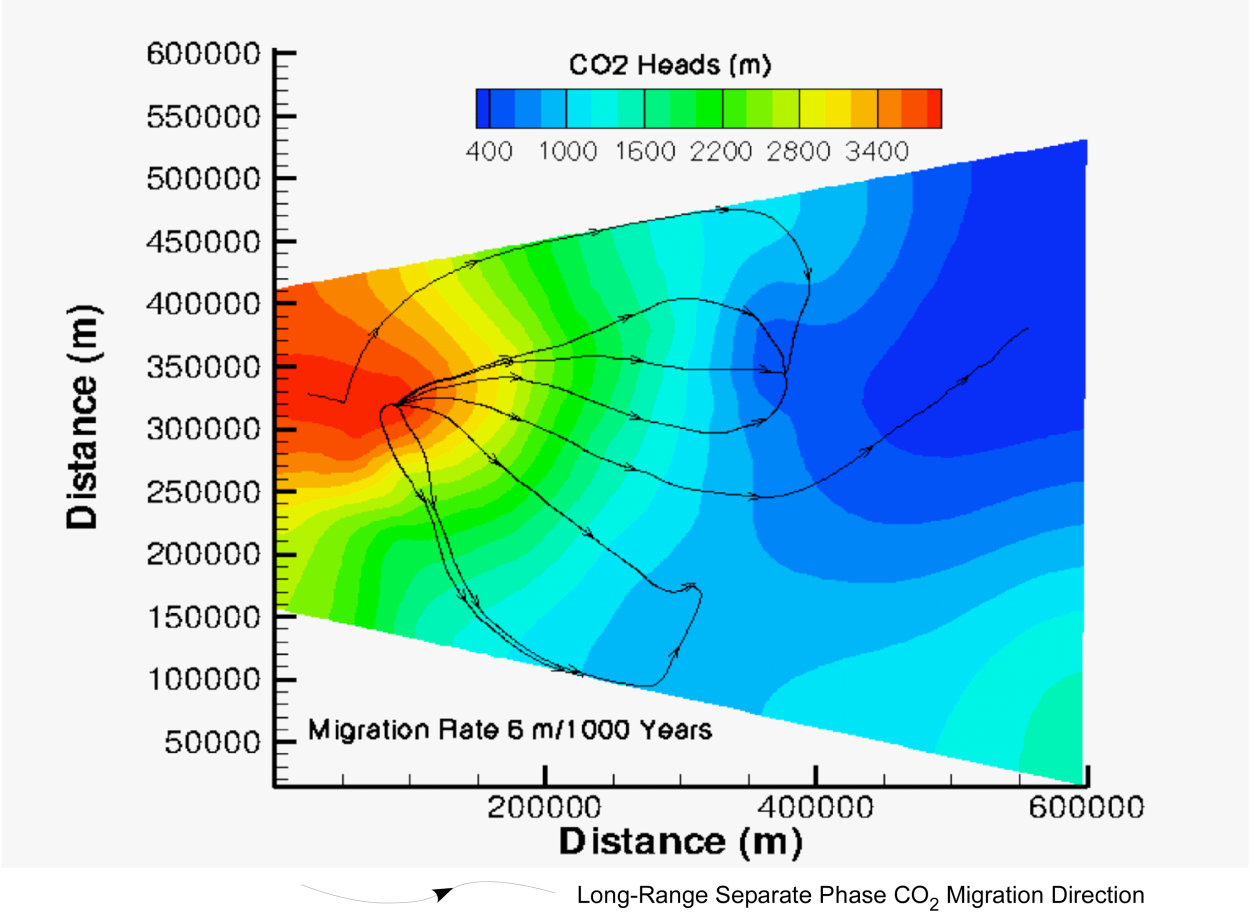
CO2 Heads (m)
400 1000 1600 2200 2800 3400
600000
550000
500000
450000
400000
350000
300000
250000
200000
150000
100000
50000
Distance (m)
Migration Rate 6 m/1000 Years
200000
400000
600000
Distance (m)
Long-Range Separate Phase CO_2 Migration Direction

Figure 22